Summer 2020

# Heterostructure of 2D Materials: HfS2/HfO2/Si

Christopher J. Robledo
*Missouri State University*, Robledo001@live.missouristate.edu

# HETEROSTRUCTURE OF 2D MATERIALS: HfS2/HfO2/Si

A Master's Thesis

Presented to

The Graduate College of

Missouri State University

In Partial Fulfillment

Of the Requirements for the Degree

Master of Science, Materials Science

By

Christopher J Robledo

August 2020

**HETEROSTRUCTURE OF 2D MATERIALS: HfS2/HfO2/Si**

Physics, Astronomy, and Materials Science

Missouri State University, August 2020

Master of Science

Christopher J Robledo

## ABSTRACT

Heterostructures have been utilized in electronic devices for over 50 years with the proposal for the first heterostructure transistor in 1957. With the scaling of devices, it is necessary to create new heterostructures that will comply with Moore's Law, as well as make devices faster and consume less power. Novel 2D materials, such as hafnium disulfide, have shown promise as an active channel layer, while hafnium dioxide is already proven to be a replacement of silicon dioxide for the gate insulating layer. However, fabrication techniques for wide-scale integration of these heterostructures have not yet been achieved. Also, the dielectric properties of hafnium dioxide must be realized before it can be used as a replacement of silicon dioxide. Dielectric spectroscopy results indicate that the dielectric constant for the samples was between 15-29, with sample 2 showing the highest dielectric constant of 28.8 and the lowest range of dielectric loss when measured from 200 Hz to 90 kHz. However, the results also indicate that proper contact of the probe with the electrodes is necessary to minimize error. Thus, the erroneous values at some frequencies could be attributed to poor ohmic contact of the probes, or a miscalibration of the system. I have also shown that hafnium disulfide layers can be created by converting some top layers of HfO2 thin films through sulfidation in hydrothermal process, thus demonstrating that creating a HfO2/HfS2 heterostructure is possible. XRD analysis shows a broad peak after sulfidation that relates to hafnium oxysulfide. In addition, the Raman analysis indicates that hafnium disulfide is present after sulfidation of hafnium dioxide.

**KEYWORDS**: thin films, heterostructure, 2D materials, hafnium disulfide, hafnium dioxide, atomic layer deposition, hydrothermal synthesis

**HETEROSTRUCTURE OF 2D MATERIALS: HfS2/HfO2/Si**

By

Christopher J Robledo

A Master's Thesis
Submitted to the Graduate College
Of Missouri State University
In Partial Fulfillment of the Requirements
For the Degree of Master of Science, Materials Science

August 2020

Approved:

Kartik C Ghosh, Ph.D., Thesis Committee Chair

Ridwan Sakidja, Ph.D., Committee Member

Tiglet Besara, Ph.D., Committee Member

Julie Masterson, Ph.D., Dean of the Graduate College

## ACKNOWLEDGEMENTS

I would like to thank my research advisor and mentor, Dr. Kartik Ghosh, for his guidance and support throughout my academic career as a graduate student. He helped me prepare for a career in the materials science industry. I will be forever grateful for his help. I would also like to thank my parents who made it possible for me to continue my education, and Sanchali Das for her help as a research partner and in my materials science studies. Special thanks to Dr. Ridwan Sakidja and Dr. Tiglet Besara for being members of my graduate committee, and for their feedback during my thesis defense. Lastly, I would like to thank Shahidul Asif for his efforts in the synthesis of the PLD-sample, and all the other faculty and graduate students who helped me throughout my academic career.

I dedicate this thesis to Sally Ann Sliwinski. Rest in peace.

## TABLE OF CONTENTS

## LIST OF TABLES

## LIST OF FIGURES

# INTRODUCTION

As we approach the limit of scaling silicon-based devices, the semiconductor field has turned its attention to 2D materials. The interest of 2D materials came about in 2004 with the discovery of graphene. Two scientists by the name of Geim and Novoselov removed some flakes from bulk graphite with sticky tape, a process now called mechanical exfoliation. Repeatedly separating the graphite fragments from the tape created a single layer of carbon atoms called graphene.[1] This discovery lead the way into the study of other materials that have a monolayer structure, such as transition metal dichalcogenides (TMDs) (e.g. $MoS_2$, $WS_2$, $MoSe_2$, $HfS_2$, and $WSe_2$), and layered double hydroxides (LDHs) (e.g. h-BN, BP). The research and development of these 2D materials has shown that they have extraordinary potential in elementary science, such as sensors, LEDs, FETs, etc. As scaling of electronic devices continues, a suitable replacement for the current and widely-used dielectric layer, $SiO_2$, will be needed due to its leakage current being too large.[2] Companies, such as Intel, have already begun the implementation of $HfO_2$ as a replacement of the dielectric layer.[3]

Hafnium dioxide ($HfO_2$, aka hafnia) is a high dielectric constant (~25) oxide that has a wide band gap (5.8 eV), high bulk modulus, high melting point (2500°C), and excellent thermodynamic stability. It can exist in a variety of phases such as monoclinic (see figure 1.1), tetragonal, cubic, and orthorhombic. At normal pressure, it can exist in the monoclinic phase at room temperature, the tetragonal phase above 2050 K, and the cubic phase above 2803 K.[4,5] According to Boscke *et al*., the stable region of the tetragonal phase extends to lower temperatures in nano-scale crystallites due to the surface energy effect. Consequently, the crystallization in thin films tends to proceed by nucleation in a tetragonal phase and a martensitic

transformation to the monoclinic phase during crystal growth. This phase transformation involves volume expansion and shearing of the unit cell.[6]

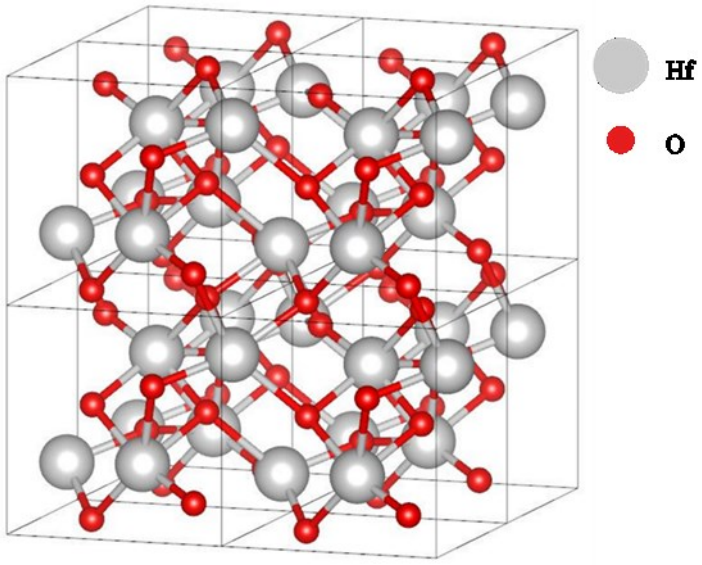


Figure 1.1: The monoclinic ($P2_1/c$, No. 14) phase of $HfO_2$. Its lattice parameters are a = 5.1126 Å, b = 5.1722 Å, c = 5.2948 Å, $\alpha = \gamma = 90°$, and $\beta = 99.18°$.

One of the requirements for a gate oxide dielectric is that it must withstand process to temperatures up to 1000°C and must not mix with the silicon channel or poly-Si gate electrode. For example, if the interfacial $SiO_2$ layer increases due to diffusion of the oxygen atoms from the $HfO_2$ layer, the dielectric constant will increase. Also, if the interfacial $SiO_2$ layer were to increase, this will add to the overall equivalent oxide thickness -which is a severe impediment to scaling of devices.[7,8]

According to Gao *et al*., thin hafnia films are often non-stoichiometric with the most prevalent defect being oxygen vacancies. Monoclinic hafnia has two non-equivalent oxygen sites. They are threefold-coordinated oxygen $O_3$ and fourfold-coordinated oxygen $O_4$. This means that it can have two different types of oxygen vacancies. In contrast, an amorphous oxide

has many advantages over a poly-crystalline oxide with one of them being the absence of grain boundaries. Grain boundaries in polycrystalline oxides act as diffusion paths for dopants. Also, since the amorphous oxide is isotropic, the fluctuations in polarization from differently oriented oxide grains will not scatter carriers.[9]

The novel semiconductor known as hafnium disulfide ($HfS_2$) is a transition metal dichalcogenide. With a theoretical band gap of 1.2 eV and a mobility of 1800 $cm^2/V{\cdot}s$, it has been noted to be a good candidate for realizing low power devices. $HfS_2$ has a hexagonal closed-packed crystal structure with a $CdI_2$-like octahedral (1T) coordination (see figure 1.2). The hafnium atoms are sandwiched between sulfur atoms, giving it an atomic layer thickness of 0.59nm. The layers are held together by Van der Waals forces, which is similar to graphene layers in graphite. As the number of layers decreases from bulk to single-layer the band gap changes from indirect to direct due to the quantum confinement effect.[10]

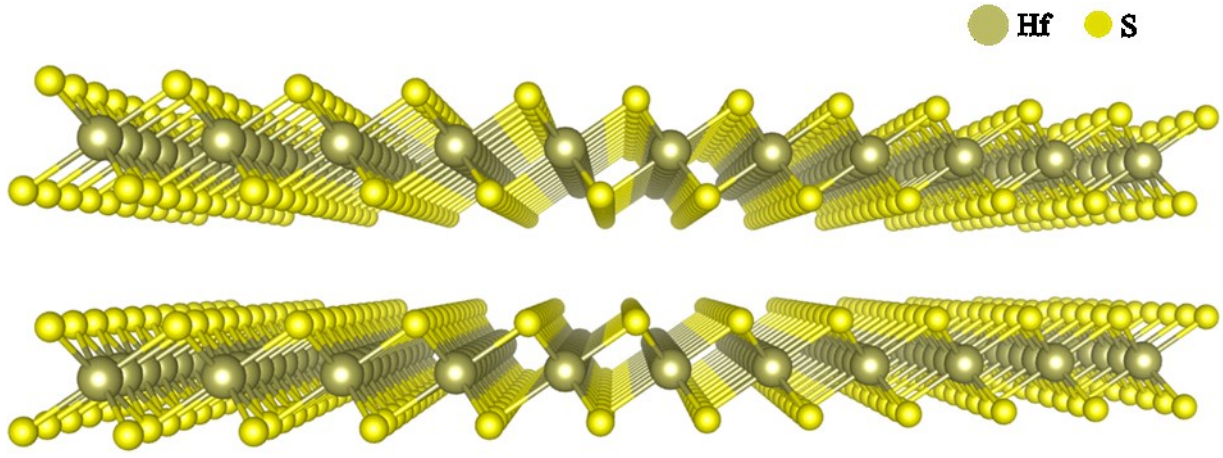


Figure 1.2: Two layers of the hexagonal ($P6_3/mmc$, No. 194) phase of $HfS_2$. Its lattice parameters are a = b = 3.3736 Å, c = 11.78820 Å, $\alpha = \beta = 90°$, $\gamma = 120°$.

The quantum confinement effect occurs when the size of the particle is too small to be comparable to the wavelength of the electron. By contrast, particles behave similar to free

particles when the dimensions of the confining structure are very large in comparison to the de Broglie wavelength. According to Ramalingam *et al*., on this stage, the energy states are continuous, and the band gap comes to its original position. The energy spectrum does not remain continuous and becomes discrete when the dimensions of the structure scales downward toward the nanoscale range. Therefore, the band gap exhibits size-dependent properties and eventually causes a blue shift of the emitted light as the particle's size is decreased. This blue shift is an increase in energy of band-to-band excitation peaks.[10]

My thesis focuses on the creation of a $HfO_2/HfS_2$ heterostructure via hydrothermal method. Hydrothermal synthesis is the process by which reactions are performed in aqueous solutions at high temperature and pressure. One possible reaction that can take place is

$NH_2CSNH_2 + 2H_2O \rightarrow H_2S + CO_2 + 2NH_3$

$H_2S \leftrightarrow H^+ + HS^-$

$2HS^- \leftrightarrow 2H^+ + 2S^{2-}$

$xS + S^{2-} \rightarrow S_{x+1}^{2-}$

$Hf^{2+} + S_{x+1}^{2-} \rightarrow HfS_2 + (x-1)S$

$HfO_2 + 2H_2S \rightarrow HfS_2 + 2H_2O$

A heterojunction with an atomically sharp interface is desirable, since the high-quality interface would result in a high FET performance and exceptional on/off ratio.[11] It is my hope that, after hydrothermal synthesis of the $HfO_2/HfS_2$ heterostructure, that an atomically sharp interface is created. In the first paper, the growth and characterization of the dielectric properties of $HfO_2$ will be discussed. And, in the second paper, the synthesis and characterization of the $HfO_2/HfS_2$ heterostructure will be discussed. The next step, after synthesis and analysis of the

data presented in this thesis, may be to utilize transmission electron microscopy (TEM) to further analyze the heterostructure.

**Dielectric Theory**

The dielectric response of a solid is its response to an electric field within it. In order to characterize the electrical properties of a capacitor later in this chapter, it is important to understand the theory behind it. First, we start with the elementary charge (q) given by

$$q = CV \quad \text{Eq. 1}$$

where C is the capacitance, and V is the potential difference. Taking into consideration our design experiment, where there is a dielectric material sandwiched between two parallel plates, we can define the capacitance (C) by

$$C = \frac{\varepsilon_r \varepsilon_0 A}{d} \quad \text{Eq. 2}$$

where $\varepsilon_r$ is the calculated relative permittivity, C is the measured capacitance at a specified frequency in Hz, d is the thickness of the dielectric material (specifically, 20 nm), $\varepsilon_0$ is a fundamental constant known as the permittivity of free space (8.85E-12 $m^{-3}$ $kg^{-1}$ $s^4$ $A^2$), and A is the area of the gold contact (specifically 2.717E-8 $m^2$ for this paper). The relative permittivity is the permittivity of the material relative to that of free space. This material property contains information about its response to an applied potential difference. Rearranging for $\boldsymbol{\varepsilon_r}$ gives us

$$\boldsymbol{\varepsilon_r} = \frac{Cd}{\varepsilon_0 A} \quad \text{Eq. 3}$$

With regards to polarization, the electric dipole moment is defined as

$$\boldsymbol{\mu} = |q|\boldsymbol{x} \quad \text{Eq. 4}$$

where $|q|$ is the magnitude of the charge and **x** is the distance between the negative and positive charges (see figure 1.3). The electric dipole occurs when two charges of opposite polarity are separated by a distance, **x**. Using the dipole moment, I can now define the polarization, which is the change in net dipole moment density produced by the applied electric field.[12]

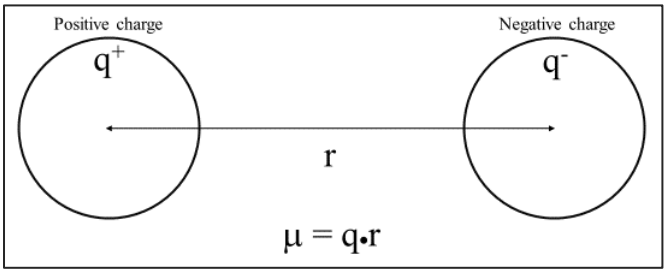


Figure 1.3: The dipole moment occurs when there is a separation of charge.

$$\boldsymbol{P} = \frac{N\boldsymbol{\mu}}{V} \qquad \text{Eq. 5}$$

where N is the number of dipoles, V is the unit volume, and $\boldsymbol{\mu}$ is the electric dipole moment. The way the material responds to an electric field can be defined by susceptibility

$$\boldsymbol{\chi} = \frac{\boldsymbol{P}}{\varepsilon_o \boldsymbol{E}} \qquad \text{Eq. 6}$$

where P is the polarization, $\varepsilon_o$ is the permittivity in vacuum, and E is the electric field. Using electric field, E, the electric displacement, D, can be defined as

$$\boldsymbol{D} = \varepsilon \boldsymbol{E} = \varepsilon_o \varepsilon_r \boldsymbol{E} = \varepsilon_o \boldsymbol{E} + \boldsymbol{P} \qquad \text{Eq. 7}$$

where $\varepsilon_r$ is the relative permittivity. The relative permittivity, also known as the dielectric constant *(k)*, is a dimensionless number related to the type of medium used as an insulator between two point charges. By solving for P, we get

$$\boldsymbol{P} = \varepsilon_o \boldsymbol{E}(\varepsilon_r - 1) = \boldsymbol{\chi E} \qquad \text{Eq. 8}$$

From this, we can see that relative permittivity is directly related to susceptibility by

$$\boldsymbol{\chi} = \varepsilon_0(\varepsilon_r - 1) \qquad \text{Eq. 9}$$

Since q = CV, it can also be shown that

$$q = CV = CEd \qquad \text{Eq. 10}$$

Plugging this into the equation for an electric field, we get

$$\boldsymbol{E} = \frac{q}{Cd} = \frac{q}{\varepsilon_0 A} = \frac{\sigma}{\varepsilon_o} \qquad \text{Eq. 11}$$

where $\sigma$ is the surface charge density. From here, relating susceptibility and polarization gives

$$\boldsymbol{\chi} = \frac{\boldsymbol{P}}{\varepsilon_0 \boldsymbol{E}} \qquad \text{Eq. 12}$$

This equation tells us that $\chi$ is directly proportional to the polarization, and that the charges related to the polarization, P, are additional charges that are induced on the parallel plates when there is a dielectric material between them, rather than a vacuum.

When there is an applied voltage across a capacitor, charge is accumulated on each plate which creates an electric field, $E_0$, assuming there is no dielectric material. If a dielectric is inserted between the electric plates, as shown in figure 1.4, then, on the surface of the dielectric, there is an induced charge between each side of the material and the parallel plate. The effective charge on each parallel plate would decrease because of the induced polarization of the material. The electric field, $E_1$, is due to the polarization of the dielectric material. This is the field of the surface charge density on the boundary of the material. Thus, the effective electric field (from a macroscopic viewpoint) can be expressed as

$$\boldsymbol{E}_{eff} = \boldsymbol{E}_0 - \boldsymbol{E}_1 \qquad \text{Eq. 13}$$

When there is a vacuum in place of a dielectric, $E_1$ is equal to zero.

So far, I have described the electric field from a macroscopic point of view. The local electric field, $\mathbf{E}_{local}$, is different from the macroscopic electric field and can be described as

$$\boldsymbol{E}_{local} = \boldsymbol{E}_0 + \boldsymbol{E}_1 + \boldsymbol{E}_2 + \boldsymbol{E}_3 \qquad \text{Eq. 14}$$

where $\mathbf{E_0}$ is the field produced by fixed charges on the surface of the parallel plates opposite of the dielectric material, $\mathbf{E_1}$ is the depolarization field from a surface charge density on the outer surface of the dielectric material, $\mathbf{E_2}$ is the Lorentz cavity field that is on the surface of a spherical cavity within the dielectric, and $\mathbf{E_3}$ is the field produced by atoms within the cavity.

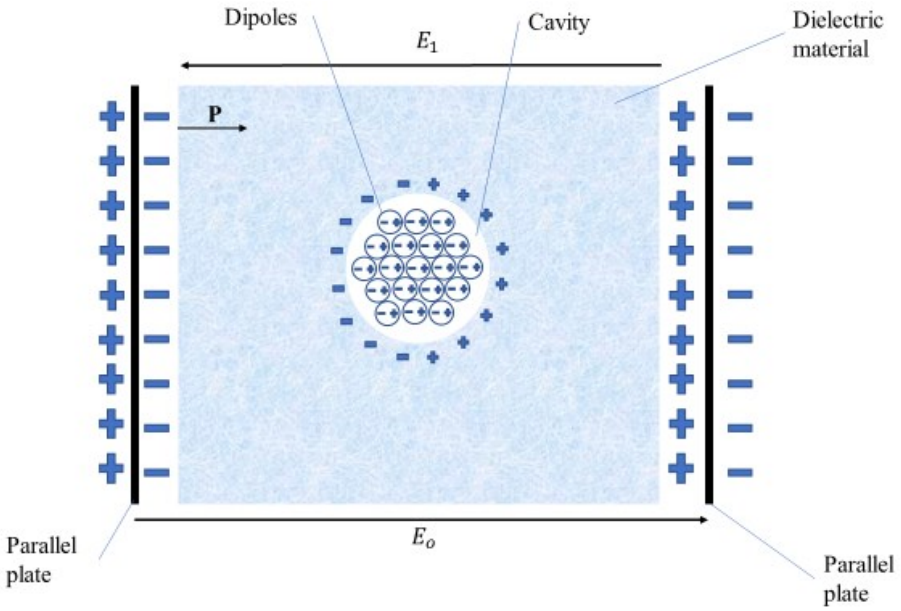


Figure 1.4: Diagram of a parallel plate capacitor and the electric field.

For polarization, replacing the static field with an *oscillating* field that has an angular frequency, ω, gives us

$$P(\omega) = \chi(\omega)E(\omega) \qquad \text{Eq. 15}$$

*where $\omega$ is equal to $2\pi f$, and*

$$E(\omega) = E_0 \exp(i\omega t) \quad \text{Eq. 16}$$

where $i$ is $\sqrt{-1}$, and $t$ is time in seconds.

To illustrate the significance of the last two equations, suppose there is a material (in thermal equilibrium) between two contact plates or electrodes, and there is no electric field present. Applying an alternating-current (AC) electric field will cause a net dipole moment density to be induced within the material. Keeping in mind that the AC field will oscillate within a specified amount of time, so, too, will the dipoles. However, the amount of time needed for the dipoles to be in equilibrium with the AC field will be much longer than the time until the sign reversal of the applied AC field. In other words, the equilibrium time of the dipoles is greater than the sign change of the AC field. Theoretically, the amount of time needed for the equilibrium of the dipoles is infinite. In practice, however, the time, $\tau$, it takes for the dipoles to align, or equilibrate, is fairly rapid. Thus, the Polarization approaches the static value.

$$P = P(0), \textit{ for } t \gg \tau \quad \text{Eq. 17}$$

If the AC field reverses sign before equilibrium is reached, then the polarization will not have reached equilibrium before the reversal of the applied field. Hence

$$P(\omega) \lesssim P(0) \text{ and } \chi(\omega) \lesssim \chi(0) \quad \text{Eq. 18}$$

This means that the equations of motion that govern the electric dipole moments after excitation is what determines the frequency dependence of the dielectric susceptibility, $\chi(\omega)$.

In the case of an oscillating electric field, the susceptibility, $\chi$, is a complex function and has two parts that can be written as

$$\chi(\omega) = \chi'(\omega) - i\chi''(\omega) \quad \text{Eq. 19}$$

where $\chi'(\omega)$ defines the component $P(\omega)$ that is in phase with the applied oscillating (or AC) field. The imaginary component of the susceptibility, $\chi''(\omega)$, is the component that is 90° out of phase.

Since $\chi'(\omega)$ defines the component $P(\omega)$, this shows that the net separation of charge is determined by $\chi'$. To understand the role of $\chi''$, the change in polarization with respect to time must be considered. The equations are as follows:

$$\frac{d[P(\omega)]}{dt} = \frac{[\chi'(\omega) - i\chi''(\omega)]d[E(\omega)]}{dt} \quad \text{Eq. 20}$$

$$\frac{d[P(\omega)]}{dt} = [\chi'(\omega) - i\chi''(\omega)]i\omega[\cos(\omega t) + isin(\omega t)]E_0 \quad \text{Eq. 21}$$

where dP/dt is the current density (current/unit area). This is also called the polarization current density. This shows that the real component of the polarization current density that is in phase with the electric field is determined by $\chi''(\omega)$. The polarization current density can be expressed as

$$J_{pol} = \chi''(\omega)\omega E_0[\cos(\omega t)] = \sigma_{AC}(\omega)E_0[\cos(\omega t)] \quad \text{Eq. 22}$$

where $\sigma_{AC}(\omega)$ is the part that contributes to the AC conductivity due to the polarization response to the electric field.

There are four types of polarization: Electronic, Atomic/Ionic, Permanent dipole, and space-charge (or interfacial) polarization. Electronic polarization occurs when the dipole moments are induced by an electric field. Atomic (or Ionic) polarization occurs only in materials whose atoms contain ionic bonds. Permanent dipole (or Orientational) polarization occurs even in the absence of an electric field. These dipoles can be randomly orientated when no such field acts upon them. However, when an electric field is applied, these dipoles will align themselves in the direction of the field. Lastly, the space-charge polarization, also known as interfacial

polarization, is produced by charge carriers that migrate through the dielectric material. Figure 1.5 shows which type of total polarization is dependent on the frequency range of the applied AC field. The dipole moment can also be defined as the product of the polarizability, α, and the local electric field of an atom. The polarizability can be related to the dielectric constant, or relative permittivity. Polarizability, α, is the measure of difficulty which the displacement can be achieved in an atom/molecule. The relative permittivity and the dissipation factor also show a frequency dependence. When considering a single electric dipole within an AC electric field, it will attempt to align parallel with the field in such a way that the polarities match with the direction of this field. As the field reverses direction, so, too will the dipole.

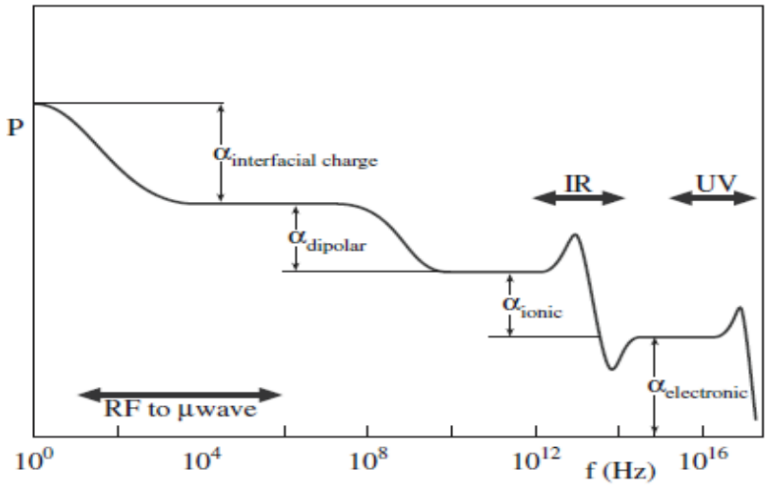


Figure 1.5: The total polarization of each type is dependent on the frequency.
Image courtesy of: http://www.uobabylon.edu.iq/uobcoleges/ad_downloads/6_8121_258.pdf

This type of behavior also applies to an ensemble of dipoles. As the frequency increases, there is a point at which the dipoles cannot "keep up" due to their inertia and the polarization will lag behind the AC electric field. This results in a reduction of permittivity of the material. If the frequency of the field continues to increase, there will be a point where the dipoles will barely

have started to move before the field reverses and try to change direction. It is at this point where the field is no longer producing any polarization on the material. The frequency at which this occurs is called the relaxation frequency because the polarization of the dipoles no longer follows the AC electric field.[13,14]

With resonance, however, there is an increase in the polarization as the frequency increases which, in turn, also means there is an increase in the relative permittivity, $\varepsilon_r'$. As the frequency continues to increase past the resonant frequency, it will reach the antiphase condition where it opposes the vibration of the charges and the polarization -as well as the relative permittivity, $\varepsilon_r'$ - will sharply decrease to a low value. If the frequency increases even further, the polarization will become steady as is shown for the ionic and electronic polarization mechanisms. The interfacial and dipolar polarization mechanisms typically don't show the resonance behavior.[12]

The permittivity also has a real and complex component that can written as

$$\varepsilon = \varepsilon' - i\varepsilon' \qquad \text{Eq. 23}$$

While the relative permittivity is used, in practice -rather than the absolute complex permittivity- it can be shown that

$$\kappa = \varepsilon_r = \frac{\varepsilon}{\varepsilon_0} = \frac{\varepsilon'}{\varepsilon_0} - i\frac{\varepsilon''}{\varepsilon_0} = \varepsilon_r' - i\varepsilon_r'' \qquad \text{Eq. 24}$$

where $\varepsilon_r'$ (the real part) is related to the stored energy within the dielectric, and $\varepsilon_r''$ (the imaginary part) is related to the dissipation of energy within the dielectric, or loss factor, and κ is the dielectric constant. Taking the ratio of the imaginary and real part of the relative permittivity gives us the dielectric loss tangent, or dissipation factor:

$$\tan(\delta) = \frac{\varepsilon_r''}{\varepsilon_r'} = \text{Dissipation Factor} \qquad \text{Eq. 25}$$

The dissipation factor, or dielectric loss tangent, is used to determine the quality of the dielectric material. The dielectric loss due to an AC field will result in the dissipation of the dielectric energy as heat. In figure 1.6, as the real part of the relative permittivity decreases sharply, there is a characteristic increase in the imaginary part.

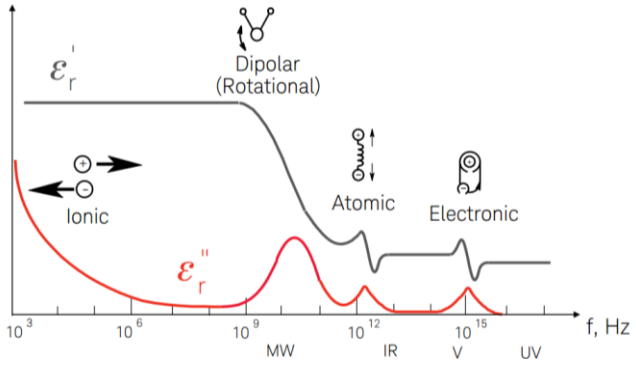


Figure 1.6: Frequency dependence of energy gain, ε', and energy loss, ε''. Image courtesy of Laughton, M. A. & Warne, D. F. Electrical Engineer's Reference Book: Sixteenth Edition. 2003

The last value that is important to the electrical characterization of dielectric materials is impedance. Impedance is the value of the opposition to all of the changing and/or unchanging current. It can be expressed as

$$Z = R + jX_C = |Z|\angle\theta \qquad \text{Eq. 26}$$

where R is the resistance, X is the capacitive reactance, $|Z|$ is the absolute value of the impedance and is equal to $\sqrt{R^2 + X^2}$, and $\theta = arctan\frac{|X|}{R}$. The capacitive reactance is defined as

$$X_C = \frac{1}{\omega C} = \frac{1}{2\pi f C} \qquad \text{Eq. 27}$$

where *f* is the frequency, and C is the capacitance. Impedance is inversely proportional to the frequency of the AC electric field. As the frequency increases, the impedance decreases until it the capacitor reaches self-resonant frequency. If the frequency were to be increased even further, the impedance will begin to rise and the capacitor will behave like an inductor, and the impedance will be directly proportional with the frequency. The phase angle, θ, is approximately -90° at the frequency below the characteristic self-resonance frequency, SRF. As the frequency increases and approaches the SRF, the phase angle will slowly climb (graphically) until it reaches 0° at the characteristic SRF. If the frequency continues to increase, the phase angle will eventually reach an angle of approximately +90°. In an ideal capacitor, the phase angle will be exactly -90°, which indicates that there is no dielectric loss.

**Raman Spectroscopy**

Raman spectroscopy is used to identify a material based on its crystal structure and molecular vibration. Raman spectroscopy is non-destructive and non-contact. Virtually no sample preparation is required, and both organic and inorganic materials in various states, i.e. solid, liquid, and gas, can be tested. A light source is used to irradiate a sample and, in turn, will generate a specified amount of Raman-scattered light that's detected using a CCD camera. Analysis of the Raman spectrum can help determine the relative amount of a material present in a sample, the thickness of the sample, the crystallinity, temperature, and whether the molecules are under compression or tension.[15,16]

Light that is incident on a molecule will scatter either elastically or inelastically. Most of the scattered light is the elastically scattered -where there is no change in energy- and is called Rayleigh scattering. A very small percentage (approximately 0.000001%), however, will scatter

inelastically. The inelastic scattering of light is called Raman scattering, which gives rise to the Raman effect. The energy of the incident light can be equal to, greater than, or less than the energy of the scattered light. If the energy of the incident light is equal to the energy of the scattered light, then the scattered light is called Rayleigh scattered light. However, if the energy of the incident light is greater than the scattered light, then the scattered light is called Anti-Stokes Raman scattered light. Finally, if the energy of the incident light is less than the scattered light, then the scattered light is called the Stokes Raman scattered light.

For the Stokes Raman scattered light, the incident light excites an electron from the ground level and then falls to a vibrational level that's higher than the ground level. As an electron falls down to the vibrational level, Stokes Raman scattered light is emitted. This light will have less energy, hence a longer wavelength, than the incident light. By contrast, the Anti-Stokes Raman scattered light will be the result of an electron excited from the vibrational level, and then falls to the ground level. Thus, the energy of the scattered light will be greater than the incident light. In the Raman spectrum, the Anti-stokes lines have less intensity than those of Stokes. It is for this reason that the Raman spectrum is composed of Stokes Raman scattered light.[15]

The range of wavelength of scattered light is associated with the different molecular bonds and vibrations. A peak appearing in the Raman spectrum will be due to a specific molecular or lattice vibration. A shift in the peak position could indicate residual stress within the crystal. The width of the peak can help determine the crystallinity of the material, and the peak intensity can help determine the concentration of the material. Taking the reciprocal of the excitation wavelength and subtracting the reciprocal of the Raman peak's wavelength will give

the Raman Shift, also known as the wavenumber. The Raman spectra utilizes a wavenumber scale ($cm^{-1}$) on the x-axis and the intensity (arbitrary units) on the y-axis. See figure 1.7.

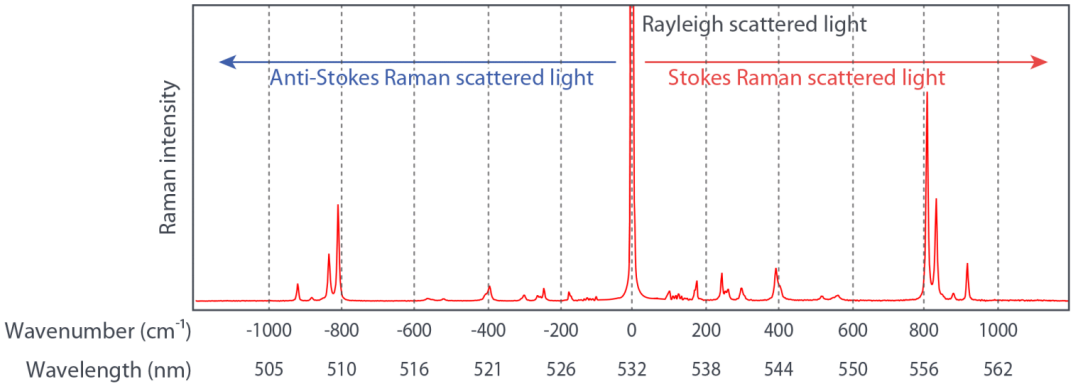


Figure 1.7: Raman spectrum of ethanol obtained by 532 nm excitation wavelength. Courtesy of: https://nanophoton.net/raman-spectroscopy

Components of a Raman spectrometer include the laser source, microscope and optics, filters, grating, and detector. See figure 1.8. The laser source provides monochromatic light that will be incident on the sample. Some wavelengths of light used for Raman spectroscopy include, but not limited to, 473 nm, 512 nm, 532 nm, 633 nm, and 785 nm. As a general rule, the higher the energy of the excitation light (lower wavelength), the less penetration depth of the sample. The microscope and optics focus the laser light on the sample and also collect the Raman signal. Typical filters are Edge and Notch filters. The filters block the laser light and allow the Raman signal to pass through. An edge filter will block all incident light up to a specified wavelength and allow all incident light past the specified wavelength to pass through. A notch filter works the same way but will also be used for Anti-stokes Raman signal. The diffraction grating disperses the Raman scattered light and projects it onto the detector. The grating consists of grooves where a higher groove density will give a wider dispersion angle. As a result, it offers a

higher resolution at the expense of coverage. In other words, when using a high-density grating, the amount of time needed to produce a Raman spectrum will increase significantly. See example in figure 1.9.

The dispersion is a function of the focal length of the monochromator and the groove density of the grating. The focal length of the spectrometer (the distance between the grating and the detector) also plays a role in the resolution. If the grating remains constant but the focal length is increased, then the higher the spectral resolution. The detector can also have an effect on the resolution. For example, a detector with a small pixel size can achieve a spectrum with a higher resolution. In summary, the factors that contribute to the spectral resolution are the widths of the entrance slit, the wavelength region where the measurement is being made, the size of the pixel on the detector, and the dispersion.

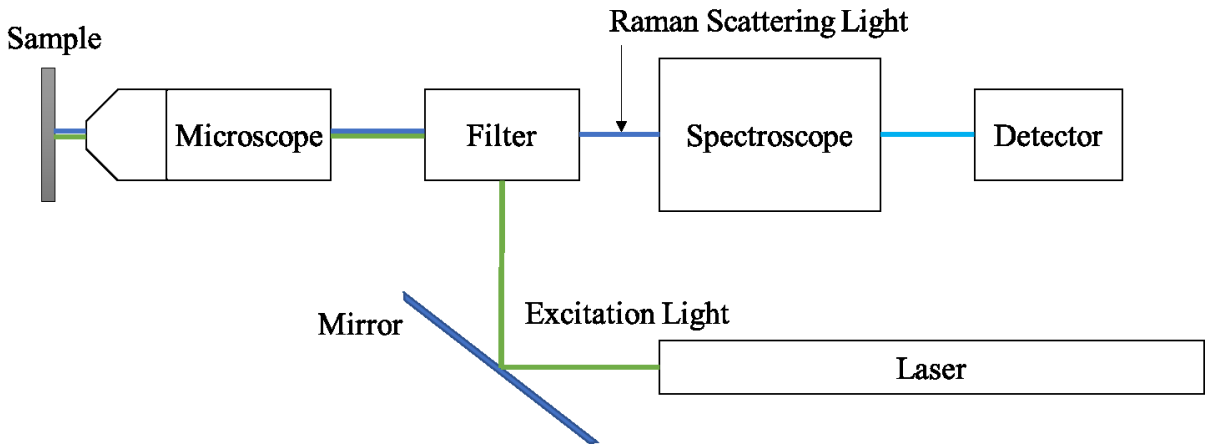


Figure 1.8: Components of a Raman microscope.

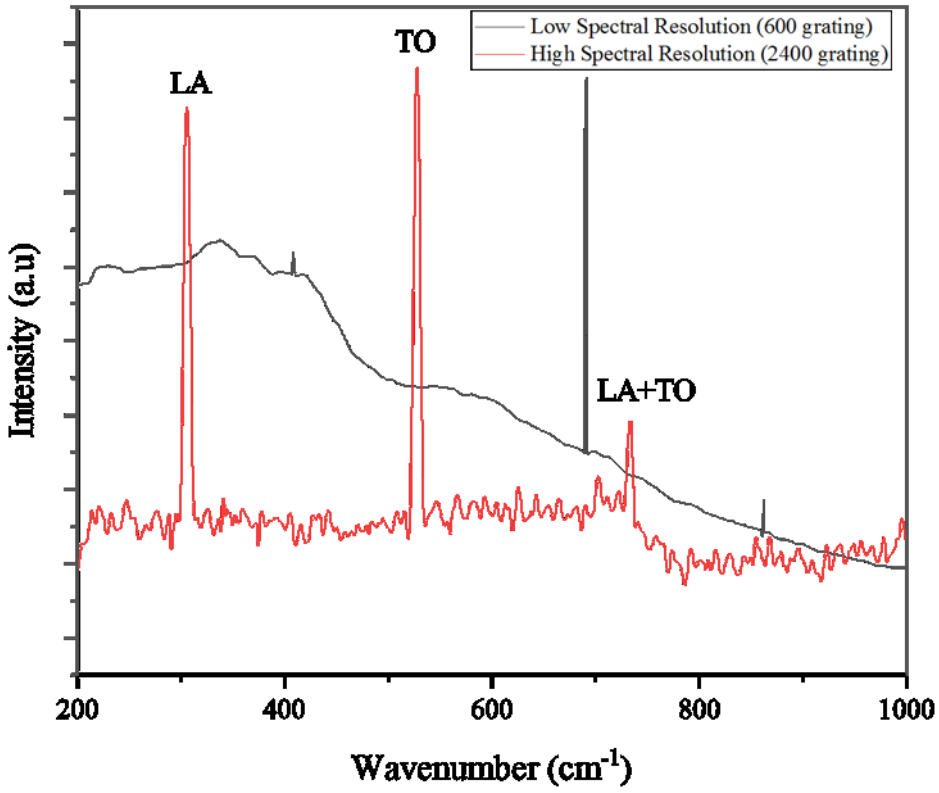


Figure 1.9: Raman spectra of $TiN_xO_{(1-x)}$ with high and low spectral resolution.

# DIELECTRIC PROPERTIES OF HAFNIUM DIOXIDE


## Abstract

Current insulating material, such as silicon dioxide ($SiO_2$), limits our ability to comply with Moore's Law, which predicts that the number of transistors within an integrated circuit doubles approximately every two years. To scale devices even further (to 3 nm), hafnium dioxide (hafnia) has shown to be a suitable replacement in the gate oxide insulating layer for complementary metal oxide semiconductor devices due to its comprehensive performance, and the ability to limit gate oxide leakage when compared to $SiO_2$. To further understand the intrinsic properties of hafnia, x-ray diffraction (XRD) analysis and electrical characterization was done on the parent and annealed samples. The XRD data shows that the most improvement in crystallinity is due to an annealing temperature at least 750°C, and not in the variation of annealing time or oxygen pressure. Electrical characterization reveals the behavior of the dielectric relaxation as a function of frequency, as well as the dielectric loss when the frequency is increased. It has also been shown that not all of the samples reached the resonance point within the measured range. Despite attempts to limit errors that may occur during electrical experimentation, it is apparent that ohmic conductivity of the probes with the contact points is crucial in obtaining good data and to minimize errors that would affect the dielectric loss. Further research should focus on increasing the frequency to the IR or optical range, and to perform C – V characterization, as well as annealing the hafnia sample at temperatures greater than 750°C and performing the standard electrical characterization technique done here.

## Introduction

Improving upon the performance of MOS transistors is crucial to the success of the semiconductor industry. In order to comply with Moore's law, which predicts the number of transistors within an integrated circuit roughly doubles every two years, scaling of these devices has shown to be an effective method in keeping with this axiom. See figure 2.1. This also allows for higher speeds, reduced costs, and lower power consumption.[17]

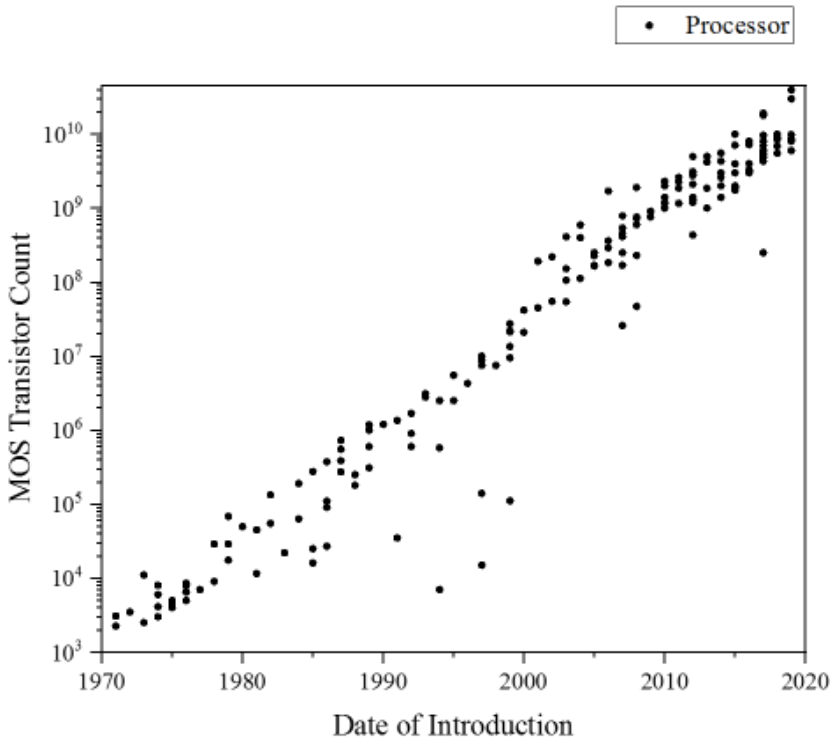


Figure 2.1: Semi-log plot of the transistor count in each processor vs the date of introduction from 1971 to 2019.

Silicon Dioxide ($SiO_2$) is the most notable material used in the manufacturing transistors. It serves as the gate dielectric due to its excellent electrical properties and the ease at which it can be synthesized. However, there are limits to the scaling of $SiO_2$. Gate leakage current is a common problem that arises when the thickness of the $SiO_2$ layer is below 1.6nm.[18] Gate leakage

current is the process by which charge carriers can tunnel through the energy barrier by way of quantum mechanical direct tunneling. High-k dielectrics (with a k value over 12, but preferably between 25-30) will allow us to use a physically thicker layer that will achieve the same performance as $SiO_2$. New materials, such as $HfO_2$, that can overcome such limitations must be researched to continue to comply with Moore's Law. In addition, $HfO_2$ films are also used as optical and protective coatings, and as a passivation layer.[19] In this paper, the dielectric properties, which are important for advanced electronic industries, have been investigated on ALD-grown thin films.[8,20]

## Theory and Experimental Methods

**Synthesis of $HfO_2$ Thin Film via Atomic Layer Deposition.** Atomic Layer Deposition (ALD) is a common method used for growing hafnia and other thin films. The growth of thin films using ALD can be realized only if the deposition process is divided into steps, and that each step is self-limiting. This self-limiting reaction must be the dominant reaction that takes place at each step. Self-limiting is when the surface reactive sites are entirely depleted, and the surface reactions will cease to occur and instead start to self-saturate. Each reaction must be self-limiting for there to be control of the atomic layers as it is grown. Due to many advantages atomic layer deposition has, it is now being introduced in the semiconductor industry as a viable solution for the processing of thin films as opposed to other techniques, such as chemical vapor deposition (CVD) and physical vapor deposition (PVD). Such advantages are the ability to control the film thickness by the number of deposition cycles, the ability to create a film as thin as 1 nm, the ability to create amorphous films, and the ability to create films that are uniform and

smooth. Some notable applications of ALD include the deposition of high-k dielectrics, electrodes, etc.[21,22]

The ALD-grown sample used throughout this paper was grown at the Wright-Patterson Air Force Research Laboratory near Dayton during the Summer of 2017. Specifics of the deposition are not available, but some parameters are known. The deposition took place at an unknown temperature with the most likely precursors being $HfCl_4$ and $H_2O$, although other precursors can also be used. For example, Katamreddy *et al.* has shown that Tetrakis-diethylamino hafnium (TDEAH) and Ozone ($O_3$) are viable precursors to produce crystalline $HfO_2$ when depositing at 600ºC. Their ALD rate was measured to be 1.1Å per cycle at a deposition temperature of 225°C.[22]

For the ALD process, the deposition occurs in cycles where each complete cycle adds approximately one layer of $HfO_2$. The final thickness of the hafnia thin film is 20nm and is amorphous with a minor monoclinic phase present. The substrate is composed of silicon and, for this deposition, an entire wafer was used as the substrate. This made it convenient to conduct additional annealing experiments as needed. See figure 2.2.

A simple description for one cycle of thin film growth using the ALD process is as follows: Flow of the first precursor, then purge, then flow of the second precursor, then purge again, and then repeat the cycle. In detail, the initial step of the ALD process is to pump down the vacuum chamber to base pressure, e.g. 5.0E-5 mbar, after inserting the silicon substrate. Once at the desired base pressure, the first precursor gas is pulsed (<1.33 mbar) into the chamber at a rate to allow it to fully react with the surface of the substrate through the self-limiting process. The unreacted precursor gas is then purged with an inert gas, such as Ar or $N_2$, revealing a monolayer of $HfCl_4$ that has reached saturated adsorption. Adsorption is the process by which

ions, atoms or molecules adhere to the surface of a solid material. It differs from absorption which is when a fluid penetrates the entire volume of a material. Next, a counter-reactant precursor, $H_2O$ gas, is pulsed into the chamber that reacts with the layer of $HfCl_4$ to produce a (mostly) monolayer of the desired film, $HfO_2$. Another purge is enacted to remove excess counter-reactant and/or byproducts leaving behind only the newly-formed hafnia layer.

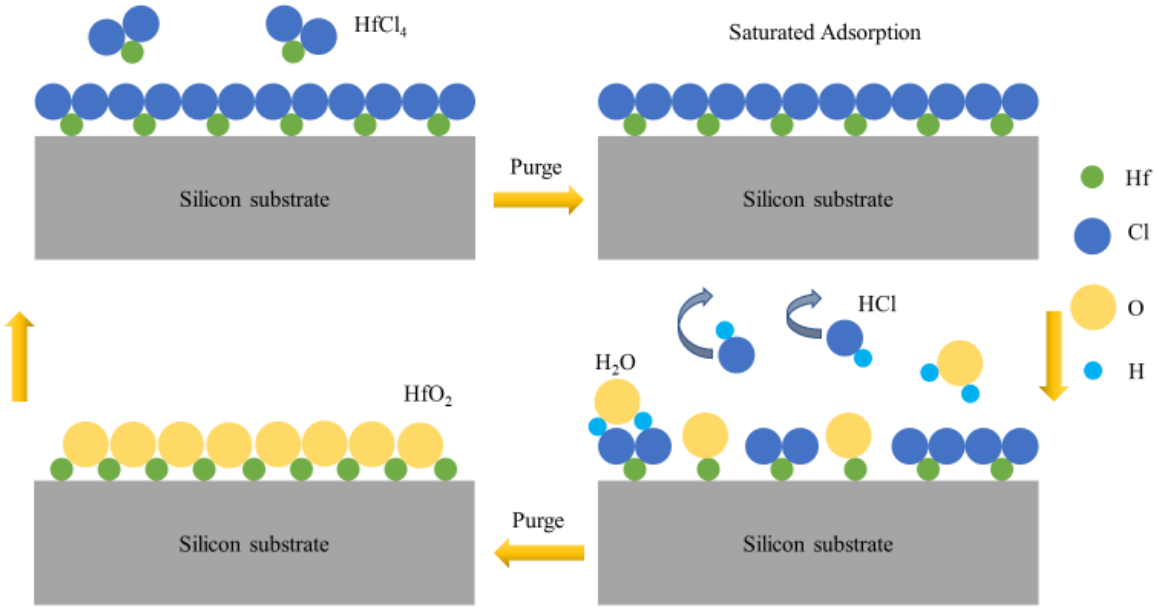


Figure 2.2: Atomic Layer Deposition cyclic process utilizing $H_2O$ and $HfCl_4$ as precursors for the fabrication of $HfO_2$ thin film on silicon.

The ALD cycle is repeated until the appropriate thickness is achieved. The chemical reaction is as follows:

$$HfCl_4 + 2H_2O \rightarrow HfO_2 + 4HCl$$

Also, there are two half-reactions that must be considered.

$HfCl_4 + 2OH_{surface} \rightarrow HfCl_2O_2 + 2\ HCl$

$HfCl_2O_2 + 2\ H_2O \rightarrow HfO_2(OH)_{2surface} + 2\ HCl$

The existing $HfO_2$ surface is assumed to be terminated by OH groups. These groups are necessary for the chemisorption of the first precursor onto the substrate. The $HfCl_4$ chemisorbs exothermically onto the OH sites by the exothermic elimination of HCl. In the second stage, water oxidizes the Cl atoms again with the elimination of HCl.[21]

The growth rate for $HfO_2$ can vary depending on the deposition temperature and pulse duration. For example, Ritala *et al.* reported a growth rate of hafnia to be approximately 0.5 Å per cycle at a deposition temperature of 500ºC. According to Widjaja *et al.* this implies that only a sub-monolayer of the film is deposited during each cycle. Justification for this statement includes the difficulty in producing a full monolayer due to steric repulsions between adsorbates and the difficulty in desorbing reaction by-products. [23,24]

**Annealing Process.** All samples are taken from the silicon wafer which has an ALD-grown, 20nm, amorphous hafnia layer on top. From this wafer, samples were cleaved for each experiment with a diamond scribe. Each sample piece was sonicated in acetone and then in alcohol for 15-20 minutes. The samples were placed in an 18" spherical vacuum chamber for annealing. Next, the chamber was pumped down to a base pressure of 5.0E-5 mbar. The ramp time to reach 600-750°C was 30-35 minutes. After reaching the desired temperature, $O_2$ gas was introduced into the system and the background gas pressure was increased to 1.0E-1 mbar. Annealing of the sample lasted between 1-2 hours at a constant pressure of 1.0E-1 mbar. When the annealing duration ended, the sample was cooled naturally to RT before removal from the chamber. Each sample was annealed at the specified parameters listed on Table 1. After annealing of S1, S2, S3, S4, and S5, X-ray Diffraction (XRD) was performed on each sample, including the parent sample.

Table 1: Annealing Parameters for all ALD-grown samples. *Errors during annealing.

| ALD-grown Sample | Pressure (mbar) | Temp (°C) | Anneal Time (hr) |
|---|---|---|---|
| Parent | As-grown via ALD | | |
| S1 | 1.00E-02 | 600 | 1 |
| S2 | 1.00E-01 | 600 | 1 |
| S3* | 1.00E-01 | 600 | 2 |
| S4 | 1.00E-01 | 600 | 2 |
| S5 | 1.00E-01 | 750 | 1 |

**X-ray Diffraction (XRD).** To study the morphology of the ALD-grown hafnia, XRD was used as a means for characterization. The X-ray diffractometer used was a Bruker AXS D8 ADVANCE with a Cu-Kα source with a wavelength of 1.5406Å. A θ-2θ scan was performed for a range of 20° – 80°. The scan speed was set to 4 seconds with a step size of 0.0196, and the sample was set to a Z-value of -0.5 mm to compensate for the adhesive and substrate thickness. An XRD scan was performed after the annealing of each sample, including parent sample.

**Electrical Measurement Procedure.** Gold dots were sputtered on the hafnia wafer at room temperature with a Cressington 108 Auto Sputter Coater. One of the gold dots acts as the top contact for the electrical probes, and a portion of the hafnia is etched away using a diamond scribe to reveal the silicon substrate that acts as the bottom contact point. The probe station probes were then connected to the two contact points with the opposite ends connected to an HP 4284A Precision LCR meter via a coaxial cable. LABVIEW was used to record the electrical measurements via a GPIB-to-USB adapter connected from the LCR Meter to the computer. No direct contact with the LCR meter was required to adjust the frequencies and record the measured values. See figure 2.3.

A voltage of 1V was applied to the system and the frequency was varied from 20 Hz to 1 MHz with a total of 45 points of data collected across the frequency range. Four values were collected for each data point: Capacitance (C), Dielectric Loss (D), Impedance (I), and Phase Angle (θ).

From the dielectric response theory described in an earlier chapter, I used Eq. 2 and Eq. 3 to calculate the relative permittivity and plot it as a function of frequency for the $HfO_2$ samples since the measured capacitance is given for the specified frequencies. The measured Dissipation Factor can also be taken directly from Eq. 25.

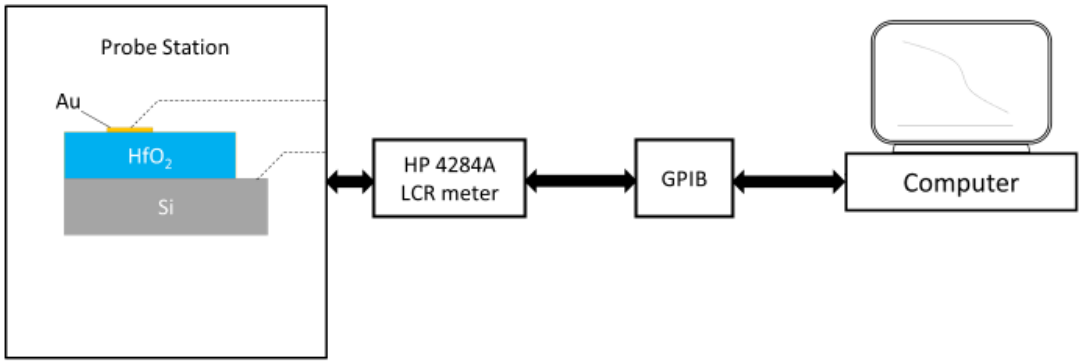


Figure 2.3: Diagram of the electrical measurement setup. (Components are not to scale.)

**Results and Discussion**

The parent sample (also called the as-deposited sample) is the result of atomic layer deposition of hafnia without any annealing. The peak shown at approximately 62.3° for the parent sample is identified with the substrate and pertains to the Cu-Kβ radiation from the X-ray diffractometer. The large, single dominant peak at 33° is identified with the silicon substrate. This peak is known as a forbidden peak and appears only under certain conditions during an XRD scan. For example, when there is distortion in the silicon lattice, or when it stems from the

Si 400 reflection of half the wavelength of the Cu-Kα radiation. Also, if there is a well-defined in-plane orientation of the sample, this may cause the (200) peak to be visible in the XRD pattern. A detailed explanation will not be discussed here, only note that this peak corresponds to the silicon substrate. From figure 2.4, after an initial annealing duration of 1 hour at a pressure of 1.0E-2 mbar and a temperature of 600°C, the monoclinic phase in the m(020) direction (at 35.8°) begins to form in sample 1 (S1). However, the majority of the thin film is still amorphous. This would indicate that adjustments need to be made in the annealing parameters to improve crystallinity.

An increase in the background gas pressure to 1.0E-1 mbar results in the growth of monoclinic peaks in other directions as shown in S2, when compared to S1. The annealing temperature and time remained the same. Since an increase in pressure did improve the crystallinity, the annealing for S4 was done at the same pressure of 1.0E-1 mbar, as was the case in S1 and S2, but the annealing time was increased to 2 hours instead of 1 hour. The increase in annealing time resulted in the increase in peak intensity of m(020) at 35.8° considerably when compared to S1 and S2. (See inset of figure 2.4.) Overall, however, the sample is still mostly in the amorphous phase despite the increase in annealing time and background gas pressure.

It's worth mentioning that an error occurred during the annealing of sample 3 (S3). After reaching 600°C, the gas valve on the vacuum chamber was opened to allow the $O_2$ gas to enter. The background gas pressure was increased to 1.0E-1 mbar and annealing was performed. However, after annealing was done, it was determined that the gas valve on the $O_2$ cylinder was not opened to allow continuous flow. Although annealing did occur as planned, oxygen vacancies will appear in greater abundance if there is an insufficient amount of $O_2$ background

gas. The background gas, in this case, was composed mostly of Air instead of $O_2$. For this reason, S3 was not included in figure 2.4.

For sample 5, the hafnia thin film transitions from amorphous to polycrystalline after annealing. The parameters are the same as S2, with the exception of the temperature increase from 600°C to 750°C. At 750°C, additional monoclinic peaks form between 30° and 53°. Also, the additional peaks are dominated by a tetragonal peak at 30.8° with an orientation of (101). With mixed phases of monoclinic and tetragonal present, it may indicate that an increase in temperature greater than 750°C would be necessary for a complete transformation of the tetragonal phase to the more stable monoclinic phase. Justification for this is discussed later in the chapter.

All peaks were indexed using the ICSD database CIF file number 27313 and 173966 along with the references that are to follow. Note that a tremendous effort was made to peak-fit this XRD data with all CIF files of monoclinic, orthorhombic, and tetragonal $HfO_2$ crystal structures. Part of the difficulty lies in the disagreement of the peak positions between all CIF files as well as the references. For example, the position of the m(002) peak for hafnia can vary up to 0.5 degrees between CIF files. At higher angles, the variation can be up to 4 degrees. Also, the m(220) and m(020) peak position shown in references are reversed when compared to the ICSD database. Unfortunately, the XRD pattern of ALD-grown $HfO_2$/Si does not show a preferred orientation as in the case with ZnO/$Al_2O_3$, or $TiO_2$/Si.

Ho *et al*. reported ALD-grown hafnia on p-type Si substrate with variation in annealing temperature ranging from 400°C to 900°C and annealing times between 30 minutes to 10 hours. The thickness of their hafnia film measured 20 nm. Their results show a resolution for all peaks except for the peak near $2\theta = 30.4°$.

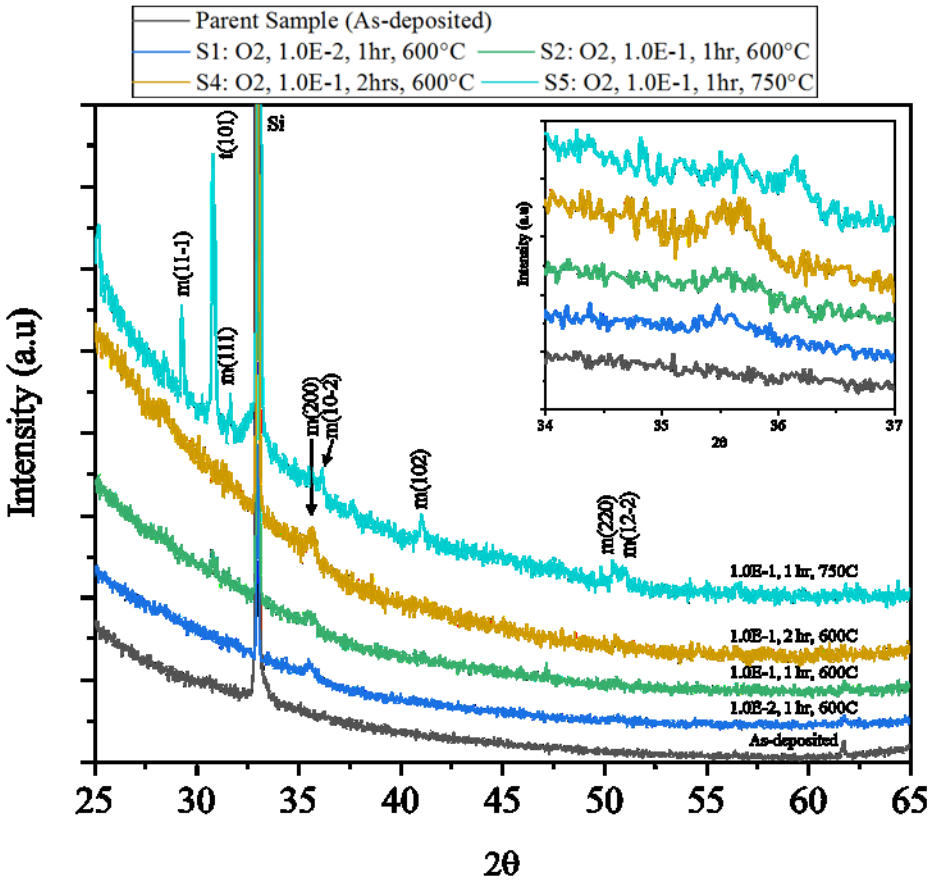


Figure 2.4: XRD plot of Parent Sample and annealed samples. Sample 3 is not included due to errors in the annealing process.

All resolved peaks are of the monoclinic phase, with the exception of the peak near 30.4° that could be attributed to either the tetragonal or orthorhombic phase. Their data shows that there could be an overlap of the phases, but state that more research is needed for confirmation. At 400°C, there is very little change in the peak intensity when annealing for 30 minutes, 1 hour, or 10 hours. However, when the temperature is increased to 900°C, the peak intensity of the monoclinic phase increases significantly, but the unresolved peak at 30.4° disappears. This would indicate that this peak is in the metastable phase, and, therefore, may be orthorhombic or tetragonal. As was the case with the previous work Ho *et al*. does not index all of the peak positions, with a couple notable exceptions. They conclude that the grain growth in the system is

thermally activated, since there was no significant change regardless of the annealing time at 900°C. The two reports agree that the orthorhombic (o-) and tetragonal (t-) phases are stable at higher temperatures, and metastable at lower temperatures. An increase in temperature will allow the o- and t- phases to transition to monoclinic (m-) at higher temperatures. The overall film structure, however, will remain polycrystalline due to the increase of the nucleation of other growth directions at higher annealing temperatures. My results are also in agreement with their work.[21]

After the XRD scan of all samples, $C-f$ measurements were conducted and analyzed. The following figures show a semi-log or log-log plot for all samples. If the axes were plotted as linear, then the capacitance will appear to decay exponentially as the frequency increases. However, as a matter of convention and visibility, the plots will show the x-axis in log scale. This also allows the data points to be evenly distributed over the entire frequency range.

In figure 2.5, the $C-f$ plots for all samples show a minor fluctuation between 40 and 70Hz (dotted circle). This fluctuation is most likely attributed to noise within the system. Also, noise attributed to a sharp peak at other frequency values, such as 100 Hz and 100 kHz. These values, with the exception of 400 kHz, were omitted from the plots.

Figure 2.6 shows the range of capacitance for all samples. The frequency range for the bar graph is between 20 Hz and the highest frequency value just before the capacitance started to increase exponentially, approximately 200 kHz. The total number of data points is between 35-37, depending on the sample. From this data, it is apparent that the capacitance range for the amorphous parent sample, and the polycrystalline S5 are nearly identical. It should also be noted that, regardless of the morphology they have the lowest values, and the difference between them is 9.2E-13 Farads.

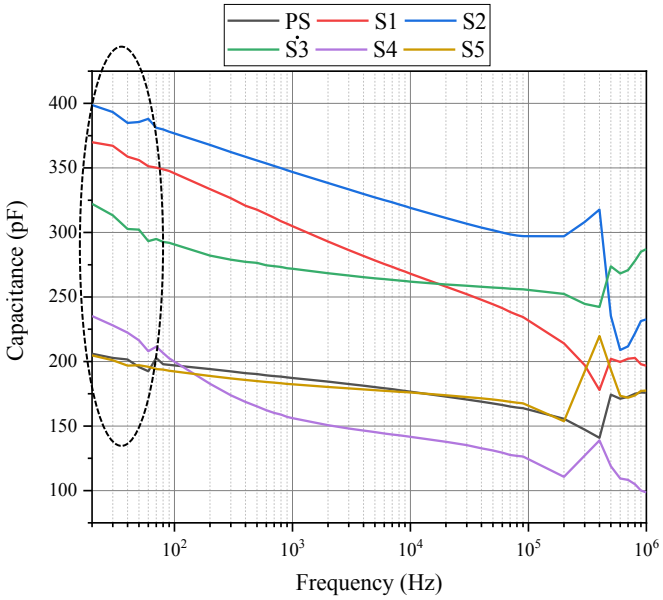


Figure 2.5: Semi-log plot of Capacitance vs Frequency for all ALD-grown samples.

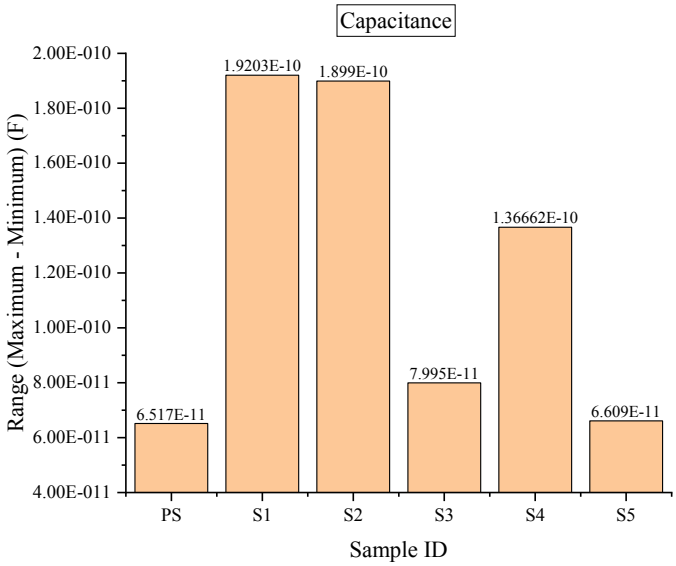


Figure 2.6: Capacitance range from 20 – 100 kHz for all samples.

Figure 2.7 shows that rearranging the capacitance equation to solve for relative permittivity (or dielectric constant) will result in a graph similar to figure 2.5. It shows that as the

frequency increases, the relative permittivity decreases -as expected- until approximately 200 kHz. Then, as the frequency is increased even further, the relative permittivity increases slightly before rapidly decreasing prior to the frequency reaching 1 MHz in S2, S4, and S5. This type of behavior can be attributed to the dielectric resonance. However, PS, S1, and S3 appear to only decrease slightly before reaching 1 MHz. In case of S3, the final relative permittivity value is higher at 1 MHz than before the increase of the relaxation peak. Also, S1 has the highest dielectric relaxation, followed by S2, prior to reaching the resonance response at higher frequencies.

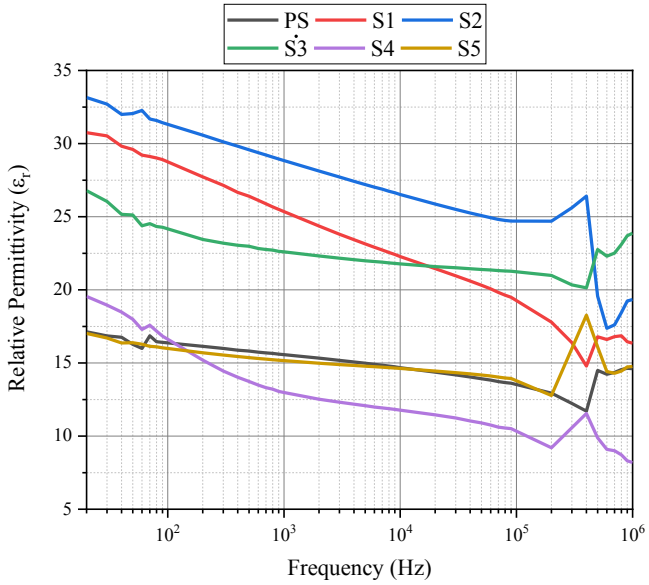


Figure 2.7: Frequency dependence of the relative permittivity ($\varepsilon_r$) from the C – f measurements.

Figure 2.8 shows the dielectric loss as a function of frequency from 20 Hz to 1 MHz. The dielectric loss for all samples is low at low frequencies and increases exponentially at high frequencies, with the exception of S4 showing a local maxima at 200 Hz. The most likely cause for this is due to poor contact of the probe with the silicon substrate. In addition to S4, S5 and the

parent sample show a slight increase in dielectric loss at the lower frequencies. The reason for this behavior is most likely due to poor contact between the probes and metal/semiconductor.

Below 1 kHz, the parent sample has the lowest dielectric loss, yet takes on a *negative* value at 400 kHz. This negative loss can be attributed to the same noise that was exhibited at the lower frequencies, and/or poor contact between the probes and metal/semiconductor points. S4 also shows the highest dielectric loss at 1 MHz and appears to continue to increase past the measured frequency range. A local maxima is not present at higher frequencies, which would suggest that a resonance response wasn't achieved, as in the case with S2 and S5.

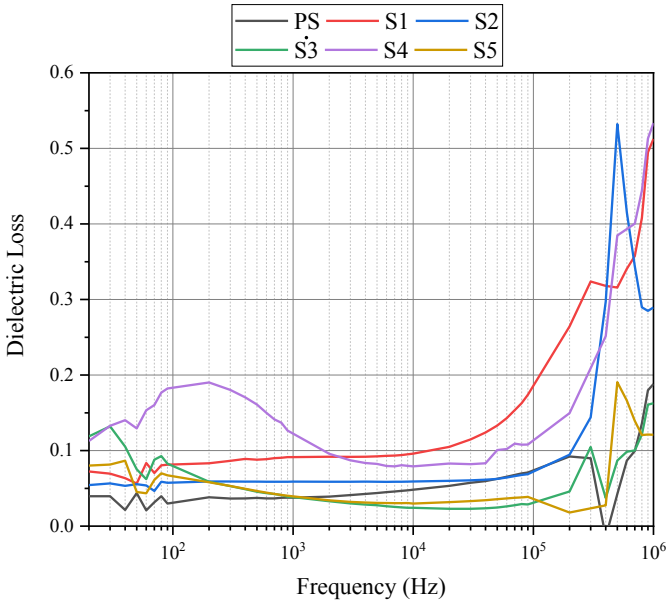


Figure 2.8: Semi-log plot of D – f for all samples.

The mean and range of dielectric loss calculated from 200 Hz to 90 kHz. See figure 2.9. (The measurements below 200 Hz were omitted due to the noise fluctuations that occurs in all samples.) Even though S2 appears to have a high mean dielectric loss, it also has the lowest standard deviation and lowest range of dielectric loss. The flat dielectric relaxation of S2 would

appear to be a significant contribution to these results, as shown in the previous figure. S4 appears to have a high standard deviation due to the wide fluctuations of dielectric loss.

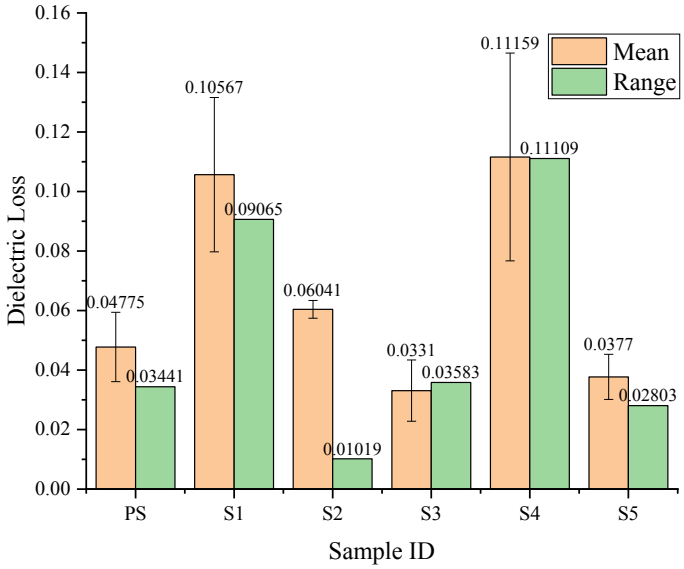


Figure 2.9: The mean and range of dielectric loss as a function of frequency measured from 200 Hz to 90 kHz.

Figure 2.10 shows the impedance as a function of frequency for all samples. While there is some minor fluctuation at the higher frequencies, no self-resonance point is found in any of the samples.

The following 10 graphs show C – D characteristics, as well as $|Z| - \theta$ characteristics. While it may seem redundant to include these figures here, textbooks and LCR manuals typically include these frequency response graphs as a matter of convenience, and to demonstrations what to expect when plotting the results.[26] Figure 2.11a shows what appears to be a resonance peak forming at 1 MHz, or higher, which would indicate the absorption of the surface (interfacial) charge polarization. Since there is a gradual increase in the dielectric loss, it can be assumed that it may also start to *decrease* beyond 1 MHz if there is, indeed, interfacial absorption occurring. Figure 2.11b shows an exponential increase in the phase angle, which may indicate that the

resonance point may appear at a lower impedance just beyond 1 MHz. Further studies into the microwave/IR frequency range would be needed to make this determination.

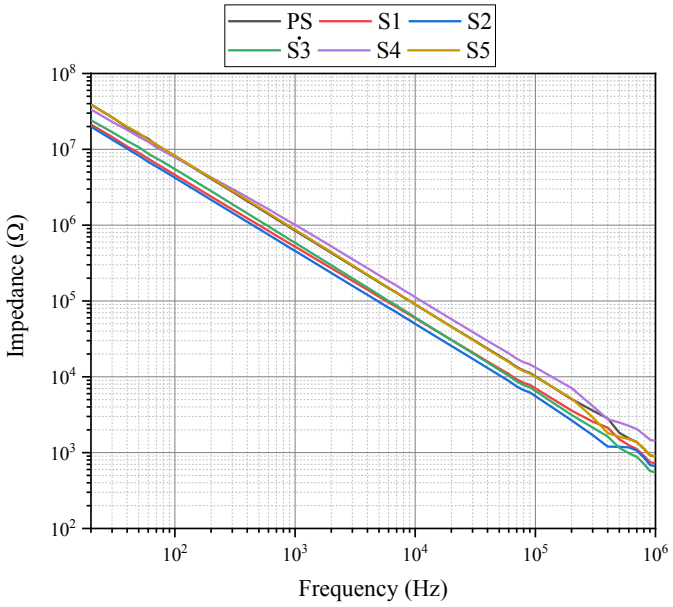


Figure 2.10: Log-log plot of Impedance vs Frequency for all ALD-grown samples.

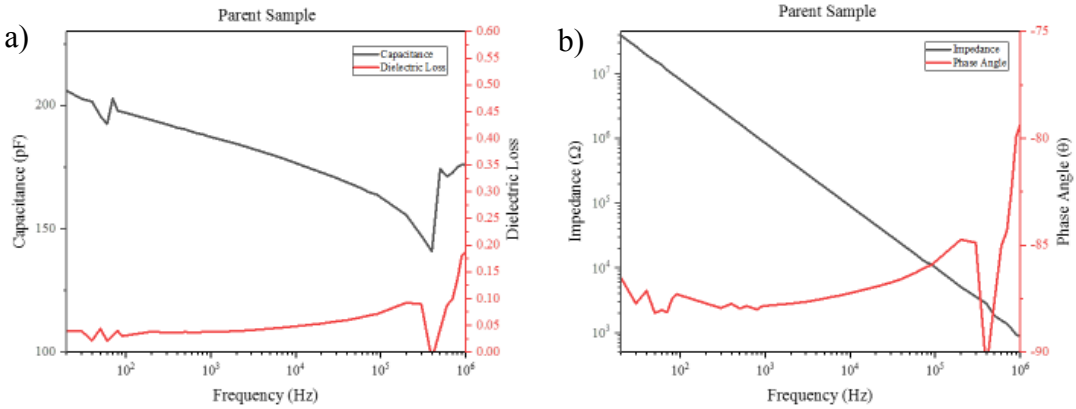


Figure 2.11: a) displays capacitance and dielectric loss vs frequency, and b) displays impedance and phase angle vs frequency for the parent sample (PS)

Figure 2.12a shows a dielectric loss that increases exponentially while the capacitance decreases linearly as a function of frequency. In figure 2.12b, the phase angle also increases

exponentially. In other words, there is a steady decrease in the polarization as the frequency increases. The resonance frequency, however, is yet to be determined.

Figure 2.13a shows an apparent resonance peak in the dielectric loss plot at a frequency of 500 kHz. In addition, the capacitance, and thus the relative permittivity, shows a negative dispersion at the higher frequency. The phase angle in figure 2.13b also shows a peak at the 500 kHz.

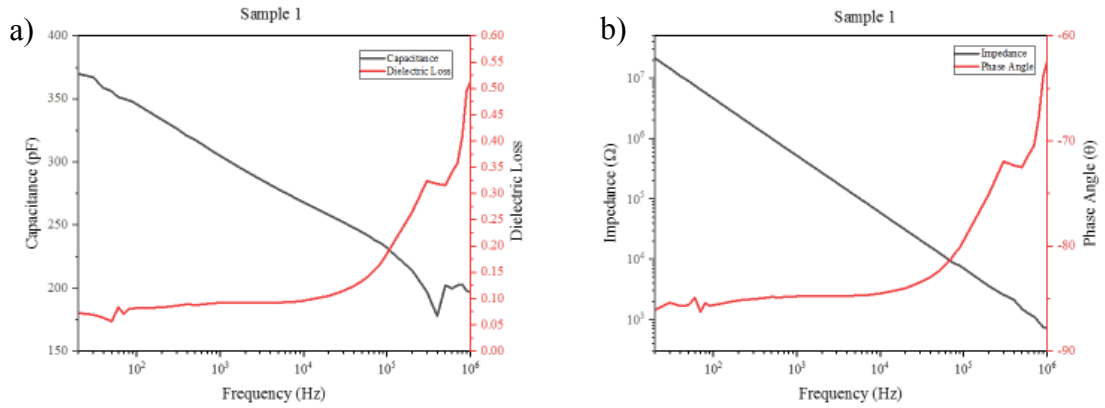


Figure 2.12: a) displays capacitance and dielectric loss vs frequency, and b) displays impedance and phase angle vs frequency for sample 1 (S1).

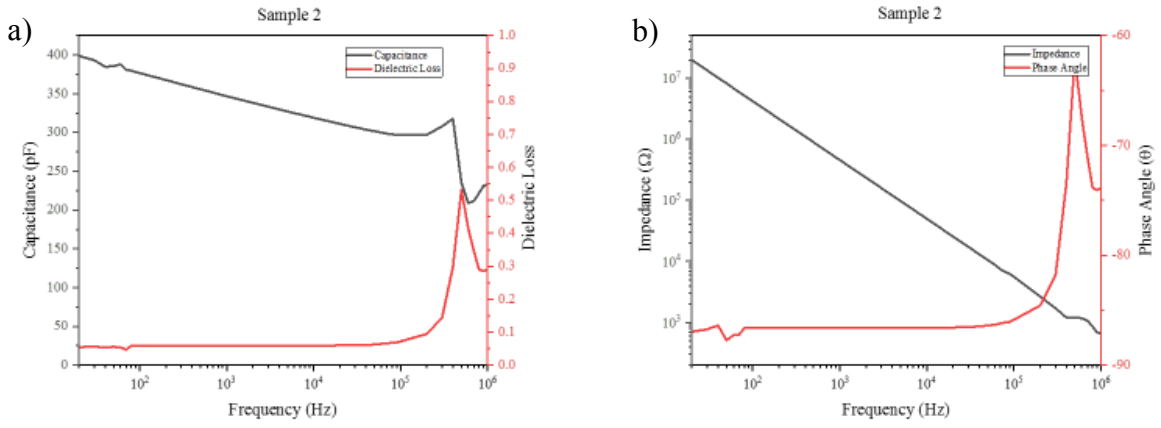


Figure 2.13: a) displays capacitance and dielectric loss vs frequency, and b) displays impedance and phase angle vs frequency for sample 2 (S2).

The dielectric loss plotted in figures 2.14a, 2.15a, and 2.16a show a negative slope at the lower frequencies, but a positive slope after approximately 10 kHz. As before, this is most likely result of a poor connection between the probe and the metal/semiconductor contact point. In figure 2.14a, there is a positive dispersion curve, since the capacitance is directly related to the complex dielectric constant, at the higher frequencies.

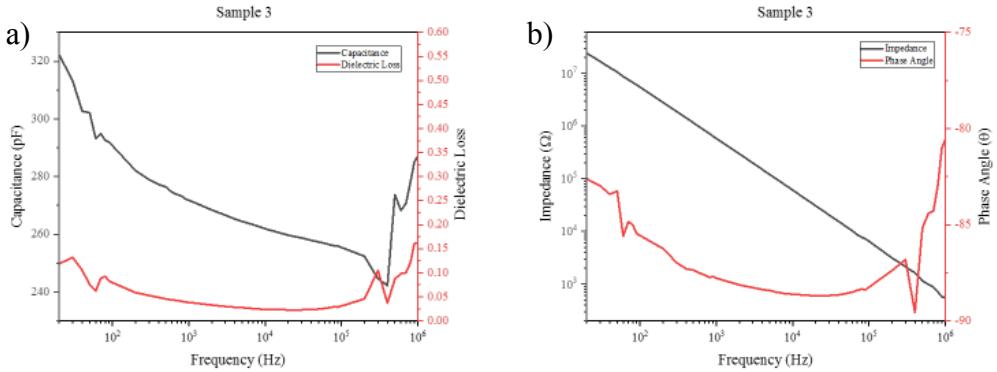


Figure 2.14: a) displays capacitance and dielectric loss vs frequency, and b) displays impedance and phase angle vs frequency for sample 3 (S3).

Figure 2.15a shows a continuously decreasing capacitance, and thus a decreasing dielectric relaxation, if the data point at 400 kHz is ignored. Also, at this frequency, the phase angle is greater than 90°. This could be due to two possibilities: 1) there is some anomalous high resistance coming from somewhere in the system (possibly from the probes), or 2) the LCR meter is not calibrated correctly. This phenomenon is also present in figure 2.16b at 300 kHz. In fact, for S5, the measured dielectric loss is negative at 100 kHz and 300 kHz. Further research is required.

Table 2 shows the measured relative permittivity for all samples at 1 kHz. From the equation, the relative permittivity is dependent on the thickness of the sample, and the area of the

electrode. The range of the reported dielectric constant of $HfO_2$ can vary anywhere from 17-25, or greater.

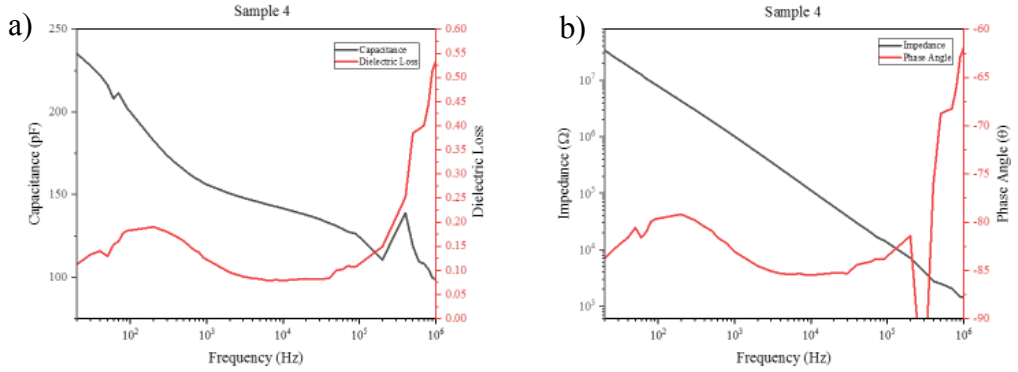


Figure 2.15: a) displays capacitance and dielectric loss vs frequency, and b) displays impedance and phase angle vs frequency for sample 4 (S4)

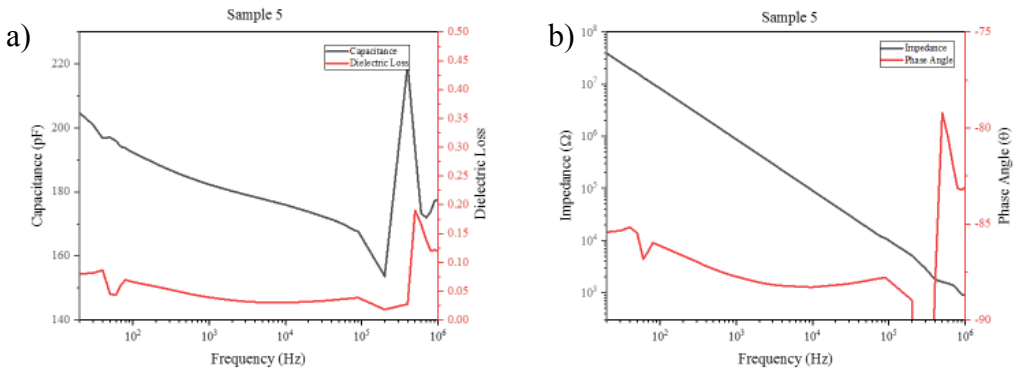


Figure 2.16: a) displays capacitance and dielectric loss vs frequency, and b) displays impedance and phase angle vs frequency for sample 5 (S5)

Robertson does not include the thickness of the oxide layer in his findings. However, Lin *et al*. reports their film thickness to be approximately 55Å with an aluminum electrode that has an area between 1E-4 and 4E-4 $cm^2$, depending on the sample. Their method of deposition for the oxide layer is ALCVD. They also reported a range of dielectric constants to be between 16 to

23, depending upon the processing conditions and the $HfO_2$ thickness, which likely due to the interfacial layer thickness.

Table 2: Measured Relative Permittivity of ALD-grown Hafnia samples and cited sources.

| Sample ID | Calculated Relative Permittivity ($\varepsilon_r$) |
|---|---|
| PS | 15.56 |
| S1 | 25.35 |
| S2 | 28.84 |
| S3 | 22.60 |
| S4 | 12.98 |
| S5 | 15.16 |
| Robertson (2004) | 25 |
| Lin *et al.* (2002) | 16-23 |

**Conclusions**

The ALD-grown hafnia samples were annealed at different temperatures. It has been shown that annealing at a temperature of 750°C improves the crystallinity of the film yet remains polycrystalline due to the nucleation of other growth directions at higher temperatures. The majority of the indexed peaks of the thin film annealed at 750°C show that the monoclinic structure has the lowest free energy since their formation is more prevalent at lower annealing temperatures, thus indicating that the monoclinic phase is thermodynamically stable at lower temperatures. Also, the annealing duration and oxygen pressure do not play a significant role in improving the crystallinity of the hafnia thin film. A metastable, high-intensity tetragonal peak forms at 750°C, which may indicate that it will require a higher annealing temperature to

transition from a tetragonal phase to a monoclinic phase. Some samples show that there is a resonance peak present before the frequency reaches 1 MHz. However, a recalibration of the LCR meter should be done to ensure that any unwanted interference, or high resistance, does not affect the results. While an amorphous film is desirable for high-k dielectrics, a slight annealing of S2 results in having the lowest range of dielectric loss from 200 Hz to 90 kHz. Further research regarding dielectric measurements should include increasing the frequency range to the IR and optical range, as well as ensuring proper contact with the probes. Also, the relative permittivity can vary depending on the thickness and area of the electrode, as shown in comparison with previously cited work, as well as the interfacial layer. TEM analysis of the interfacial $HfO_2$/Si layer should be conducted in future works to better understand the importance of this layer pertaining to the crystal structure of $HfO_2$ resulting from annealing at higher temperatures and the relative permittivity as it applies to MOS devices.

## HETEROSTRUCTURE OF 2D MATERIALS CONSISTING OF HfO2 AND HfS2


### Abstract

Since the discovery of graphene, there has been a great interest of other 2D materials, including transition metal dichalcogenides (TMDs). Among all TMDs, $HfS_2$ is predicted to have a high carrier mobility (1800 $cm^{-2}$ $V^{-1}s^{-1}$ ) and a finite band-gap (1.2eV) making it a viable candidate as an active channel layer for MOS devices.[27] However, there is no established fabrication process to synthesize $HfS_2$ on a large scale. Current techniques to produce few layers of $HfS_2$ on insulator include mechanical exfoliation and chemical vapor deposition. To address this issue, I hope to show that sulfidation of hafnium dioxide ($HfO_2$, aka Hafnia) to create layers of $HfS_2$ via hydrothermal synthesis is a viable method for large-scale usage in the fabrication of $HfO_2$/$HfS_2$ heterostructures. After sulfidation and annealing of my samples, the resulting layers were characterized using X-ray diffraction (XRD) and Raman spectroscopy. The XRD results show that the broad peak at ~71° indicates a hafnium oxysulfide layer after 8 and 16 hours of sulfidation. However, through Raman analysis, the characteristic first-order Raman modes of $HfS_2$ are present in the ALD samples, and additional second-order Raman modes are present in the PLD-grown sample. This would indicate that sulfidation via hydrothermal synthesis is a successful method in replacing oxygen atoms with sulfur by way of diffusion mechanism.


### Introduction

Current technological advancements in the field of Materials Science have enabled us to create devices that make our lives easier. Since the discovery of graphene, there has been new research in the area of thin films which have the potential to decrease device size, and lower

power consumption and cost while increasing speed and efficiency. However, before applying these materials to existing device structures, they must be fabricated and characterized to better understand their extrinsic properties, and the effect they will have with existing materials. A comprehensive understanding of these materials will enable us to realize their potential in various applications including electrical, medical, and optical devices.

The most notable of 2D materials are TMDs such as $HfS_2$, $NbS_2$, $TiS_2$, $MoS_2$, and $WSe_2$. Monolayer h-$HfS_2$ is of particular interest due to it exhibiting a direct band gap of 1.2 eV and a carrier mobility of ~1800 $cm^2/V{\cdot}s$. Some applications of this semiconducting material include photodetectors, gas sensors, and transistors. Some also require the same mechanical exfoliation technique used with graphene for fabrication. Mechanical exfoliation, also known as the "scotch-tape" method, is when a piece of polymer tape is applied over the sample and then peeled off to obtain a few layers of materials. Kanazawa *et al.* utilized this method in the fabrication of their MOSFET device. Prior to mechanical exfoliation the oxide surface was pre-treated with UV/ozone cleaner to remove any organic contaminants, and to facilitate the contact between the $HfS_2$ and $Al_2O_3$ layer. Although the thickness of their $HfS_2$ layer wasn't directly measured, they approximated it to be between 4-6 layers (2.4-3.6 nm) based on color, brightness, and contrast compared to previous studies.[28]

Lai *et al*. utilized a combination of mechanical exfoliation and chemical conversion in the fabrication of their $HfO_2/HfS_2$ hybrid heterostructure. The $HfS_2$ flakes were exfoliated onto $Si/SiO_2$ substrate with a thickness of ~25 nm. To synthesize their gate oxide dielectric, $HfO_2$, a chemical conversion of $HfS_2$ to $HfO_2$ process was used. This chemical conversion is driven by plasma oxidation of the top layer of $HfS_2$. Lai *et al*. reported an atomically sharp and defect-free $HfO_2/HfS_2$ interface with high FET performance that has an on/off ratio greater than $10^7$.

However, utilization of mechanical exfoliation for the creation of $HfS_2$ layers is still required for the synthesis of the $HfO_2/HfS_2$ heterostructure.[11]

To overcome the challenges of integrating 2D materials into MOS devices, another method in the form of hydrothermal synthesis may be the solution. Hydrothermal synthesis is a method commonly used in the study of hydrogen evolution reaction (HER). In fact, thiourea, thioacetamide, and L-cysteine are all viable sulfur sources used in the synthesis of TMDs via this method. According to Sahu *et al*., thiourea is the simplest and one of the most reactive sulfur compounds. Although thioacetamide has been used in the synthesis of $VS_2$, it is Lu (2013) *et al*. that used thiourea in the synthesis of the $Mo/MoS_2$ heterostructure. The significance of this work is that it closely matches our experimental parameters. With 0.5g of thiourea dissolved in 36mL of DI $H_2O$, the solution was put in an autoclave along with a Molybdenum foil. The autoclave was heated for 4, 8, 12, and 24 hours at 180°C. From their TEM results, the thickness of their $MoS_2$ film increased from 400 nm to 1.3μm by extending the reaction time from 4 hours to 24 hours due to more $MoS_2$ forming on the Molybdenum surface. Also, the film comprised mostly of nanosheets with the size of several micrometer, which they term to be consistent with the layered structure of $MoS_2$. They also determined the majority of the surface as amorphous, implying a high defect concentration of the nanosheets. Their XRD results did not indicate any characteristic peaks for $MoS_2$.[29,30]

In my experiment, the goal is to produce hafnium disulfide ($HfS_2$) on hafnium dioxide ($HfO_2$, aka hafnia) by way of diffusion as the mechanism for the replacement of oxygen with sulfur via hydrothermal synthesis. Once created, the samples were characterized using X-ray Diffraction (XRD) and Raman spectroscopy. The parameters for the ALD-grown sample are listed in table 3. Figure 3.1 shows the flowchart for the synthesis process. sample 5 and sample

16 were annealed, then sulfidised. Sample 16, however, had an additional step of a final annealing. Sample 18 skipped the initial annealing process and undergone sulfidation. Afterwards, the final annealing process took place. The PLD-grown sample was sulfidised after synthesis without any final annealing. The ALD-grown samples were characterized using a Bruker D8 Advanced X-ray diffractometer and a Horiba LabRAM HR Raman Microscope.

Table 3: Annealing & Sulfidation Parameters for ALD-grown samples.

| ALD-grown Sample ID | Sample 5 | Sample 16 | Sample 18 |
|---|---|---|---|
| Anneal (in $O_2$ at 750°C) (hours) | 1 | N/A | 1 |
| Final Anneal (in Ar at 500°C) (hours) | N/A | 1 | 1 |
| Sulfidation Temperature (°C): | 180 | 180 | 180 |
| Sulfidation Time (hours) | 16 | 8 | 8 |
| Precursor Solution (for sulfidation): | 130mg (0.1M) of Thiourea in 17.5mL of DI H2O | | |

The naming sequence of the samples appears to be rather awkward. The origin of samples 1 to 4 was explained in chapter 2. However, for samples 6 to 15, other attempts at sulfidation were made in which the growth deposition was done via PLD. Some of those thin films consisted of Hf/HfO2 layers and sulfidised using similar parameters as described by Lu (2013) *et al* where the amorphous Hf layer was converted to $HfS_2$ via hydrothermal synthesis. Other parameters included varying the sulfidation time and/or temperature. However, in the interest of time, those results will not be included in this paper. Sample 17, 19, and 20 are also omitted from this paper either due to errors during synthesis or the results require further analysis.

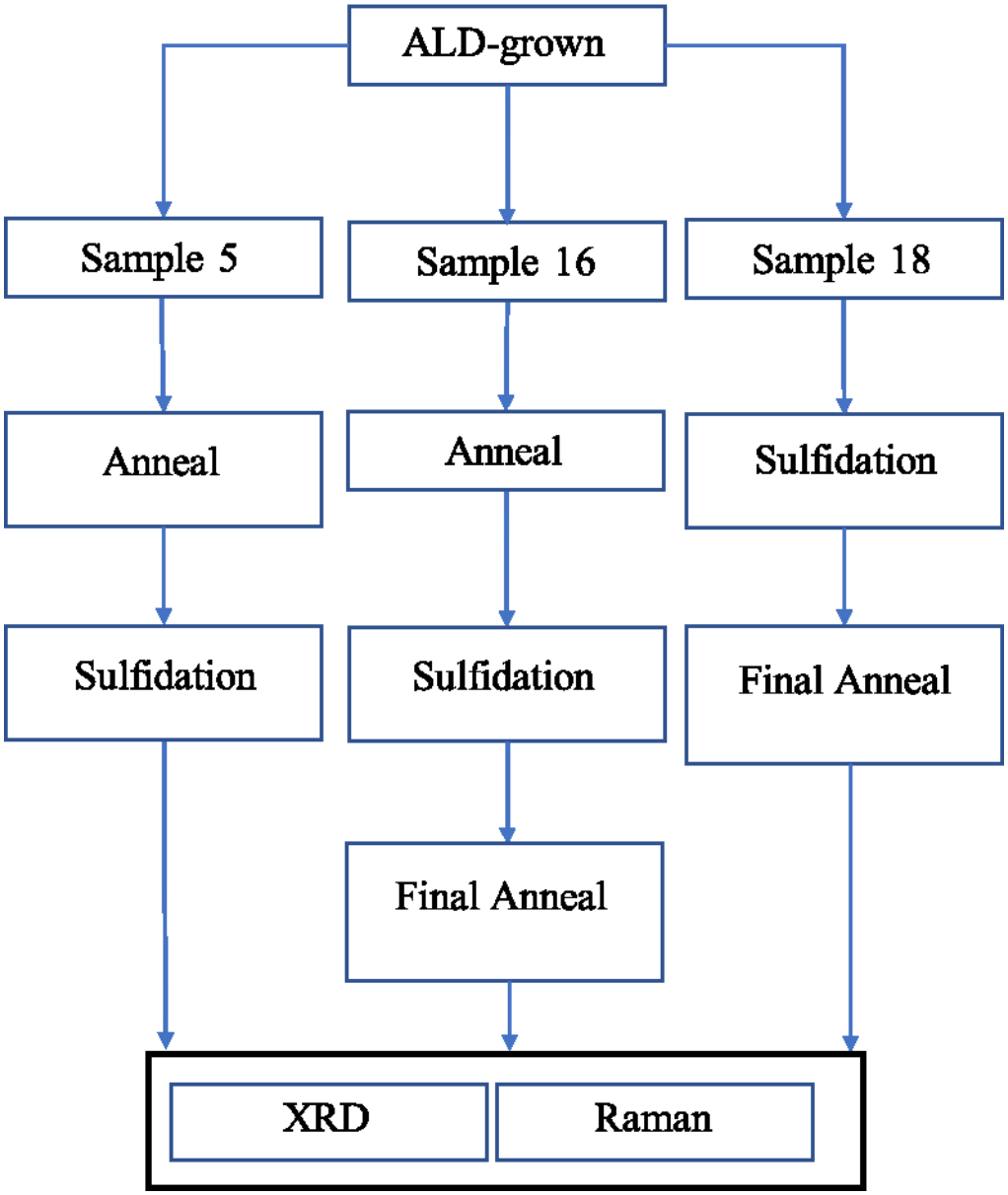


Figure 3.1: Workflow for the ALD-grown samples

**Synthesis of $HfO_2$ Thin Film via Pulsed Laser Deposition.** Although only one hafnia sample was grown using PLD, it is important to discuss the synthesis process. The synthesis of hafnia on sapphire ($Al_2O_3$) substrate via pulsed laser deposition was performed in a 12" spherical vacuum chamber which consists of the following main components: Gas inlet valve, focusing

lens, port with quartz window, substrate holder/heater, pressure gauge, target holder/carousel, roughing pump, and turbomolecular pump. See figure 3.2. Oscillating the target allows the laser pulses to ablate the target evenly.

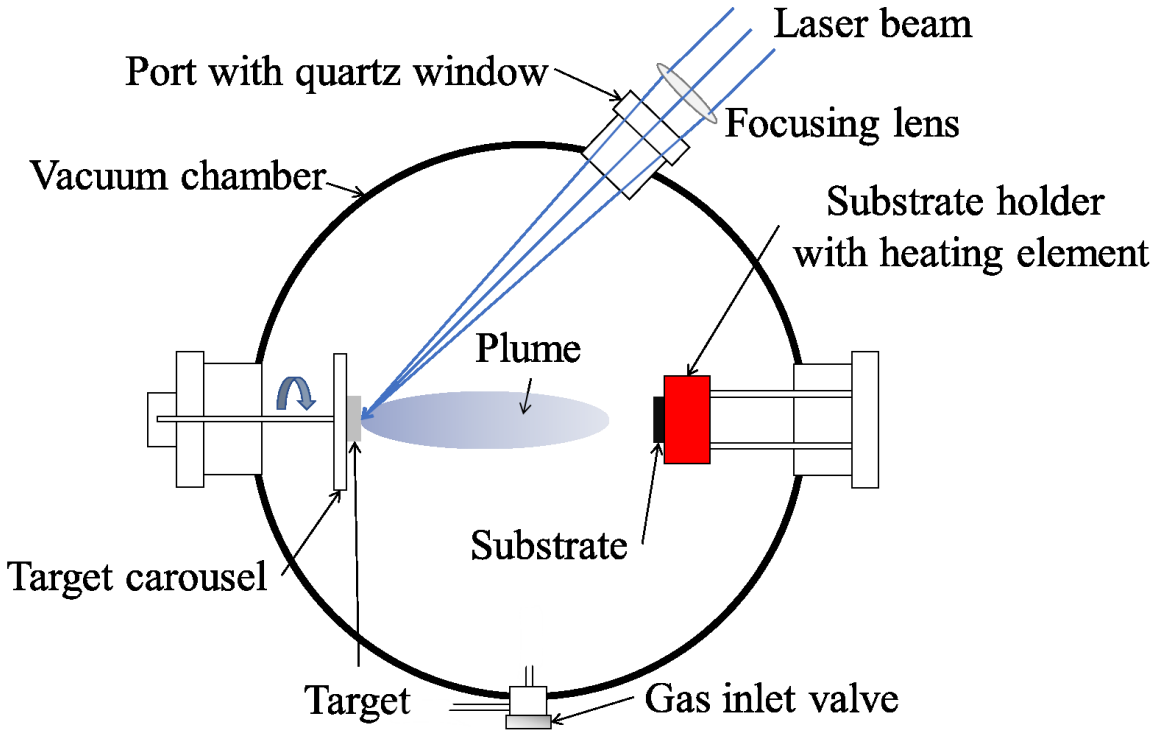


Figure 3.2: Schematic of a PLD chamber.

Once the substrate is situated on the sample stage, the chamber is pumped down to a base pressure of 5.0E0-5 mbar prior to deposition. As soon as the chamber reaches the desired base pressure, the substrate sample is then heated to a desired temperature with a ramp time of 30 minutes. After the deposition temperature is reached, $O_2$ gas is introduced into the chamber, and the pressure is increased to 1.0E-1 mbar. This pressure is maintained throughout the deposition process. The target and substrate are now ready for deposition. A hafnium target is first cleaned by ablating it with 500 shots, then ablated with an additional 20,000 shots with an average laser

energy of 125 mJ/pulse from a neodymium-doped yttrium aluminum garnet (ND:YAG) nanosecond pulse laser. The laser energy density was approximately 3mJ/cm$^2$, and the pulse frequency was set at 10Hz with a Q-switch delay of 10μs. A film consisting of hafnium and oxygen to form hafnium dioxide forms on the top layer of the sapphire ($Al_2O_3$) substrate. After deposition, the sample is cooled down to room temperature and sulfidised for 8 hours.

**Sulfidation of $HfO_2$ via Hydrothermal Synthesis.** For the conversion of hafnia to the transition-metal dichalcogenide, hafnium disulfide ($HfS_2$), a process known as hydrothermal synthesis was used. Hydrothermal synthesis refers to the heterogeneous reactions in aqueous media above 100°C and 1 bar. ALD-grown and PLD-grown samples were both sulfidised using the hydrothermal synthesis process for various times and temperatures, depending on the sample.[31,32]

The ALD-grown samples were placed in an autoclave after cooling to room temperature due to annealing. The PLD-grown sample was placed in the autoclave after cooling to room temperature due from synthesis. One-hundred thirty milligrams (0.1M) of thiourea was dissolved in 17 mL of DI $H_2O$ by sonicating it for 20 minutes. The sonication time ensured that all the thiourea dissolved in the solution prior to hydrothermal synthesis. After sonication, the precursor solution was poured into an autoclave as shown in figure 3.3. The autoclave is then sealed with a Teflon cap, spring, and stainless-steel cap. Next, it is placed in a furnace and sulfidised for 8 hours or 16 hours (depending on the sample). Both sample 16 and sample 18 have a sulfidation time of 8 hours, while sample 5 has a sulfidation time of 16 hours. The hydrothermal synthesis temperature for all three samples was 180°C. After sulfidation, the next step for each sample is outlined in the flowchart above (See figure 3.1).

After the PLD sample was grown, 0.1M of thiourea was dissolved in 17.5 mL of DI $H_2O$. The solution and sample were put in the autoclave and sulfidation took place for 8 hours at a

temperature of 180°C. After sulfidation, the sample was allowed to cool to room temperature and then characterized with a Renisaw inVia Qontor confocal Raman microscope at the Wright-Patterson Air Force Research Laboratory.

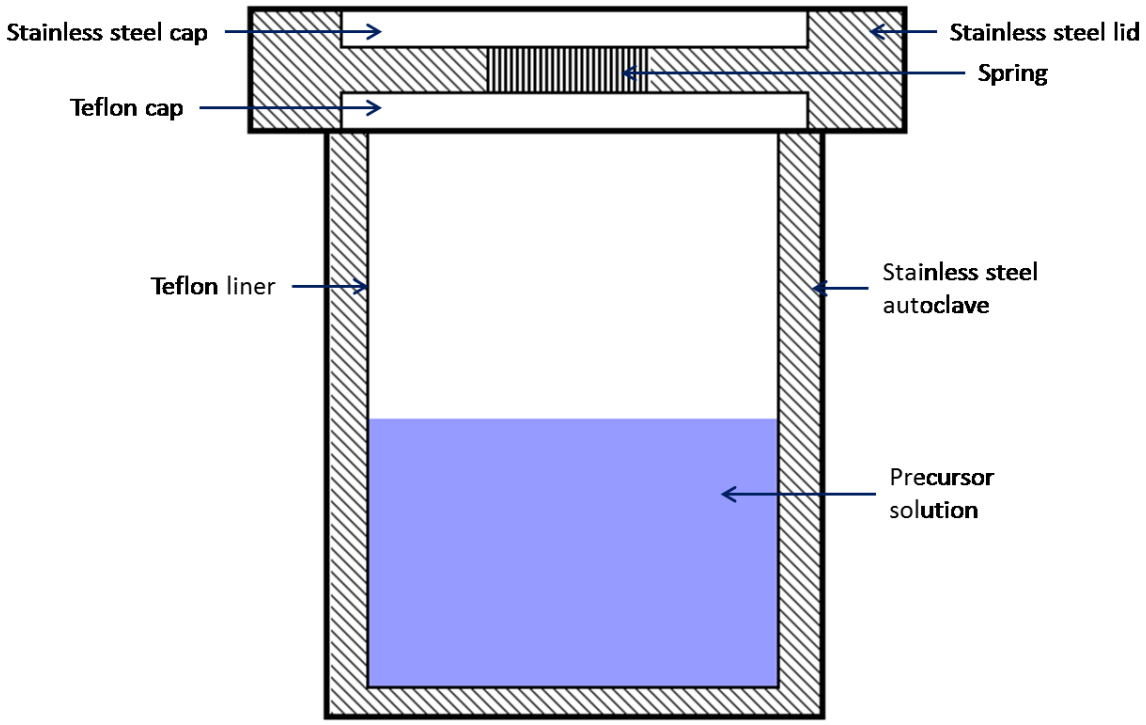


Figure 3.3: Diagram of an autoclave for hydrothermal synthesis

**Results and Discussion**

All $HfO_2$ peaks were indexed using the ICSD 23327 CIF card. The XRD results in figure 3.4 show that the as-grown parent sample is mostly amorphous with a minor monoclinic peak at ~76.3° (20-4). The substrate XRD pattern from the parent sample shows a Cu-Kα silicon doublet peak at 69.6° (400), a Cu-Kβ silicon peak at 62.33°, and a Cu-Kα peak at 33°. The nearly vertical slope that begins at ~67° is characteristic of the silicon substrate, as it was also reported by Okamura *et al*.[33] The silicon peak at 33° is known as the forbidden peak. This peak occurs

due to special conditions that are met during an x-ray diffraction θ-2θ scan. It may not always be present, especially after sulfidation of the sample. Specific details of the forbidden peak are discussed in chapter 2 and elsewhere.[34] After annealing sample 5 at 750°C for 1 hour in $O_2$ gas at 1.0E-1 mbar, the ALD-grown, amorphous hafnia on silicon transitions to polycrystalline with monoclinic growth in multiple directions. The indexed peaks of the annealed sample (sample 5) are monoclinic except for a single, dominant peak at 29.5°, which is tetragonal. At 750°C, the two monoclinic peaks decrease in intensity while additional monoclinic peaks form between 30° and 53°. The additional peaks are dominated by the tetragonal peak at 30.8° with an orientation of t(101). With polycrystalline monoclinic and tetragonal phases present, it may indicate that an increase in temperature would be necessary for a complete transformation of the tetragonal phase to the more stable monoclinic phase. He *et al*. has shown this to be the case. They reported a tetragonal peak at ~31°, but a complete phase transformation to monoclinic at temperatures greater than 700°C. At the same time, their m(111) peak at ~32° increased in intensity as the temperature was increased to 1000°C.[25]

After sulfidation, all monoclinic and tetragonal peaks disappear, and the thin film takes on an amorphous structure. There is also no indication that the hafnia thin film converted to hafnium disulfide, or if any sulfur is present within the film. The most likely peak position of hafnium disulfide would occur at ~72°, as indicated by the ICSD 43203 CIF card.

After annealing for 1 hour at 750C in $O_2$ (at 1E-1 mbar) atmosphere, sample 16 in figure 3.5b shows a highly dominant, metastable orthorhombic phase at ~25.8° in contrast with sample 5, with the rest of the XRD plot showing a mostly amorphous phase. Analysis of the orthorhombic peak (with ICSD 79913 CIF card) in figure 3.5b shows that it can have a direction of o(201) or o(111), or a combination of the two.

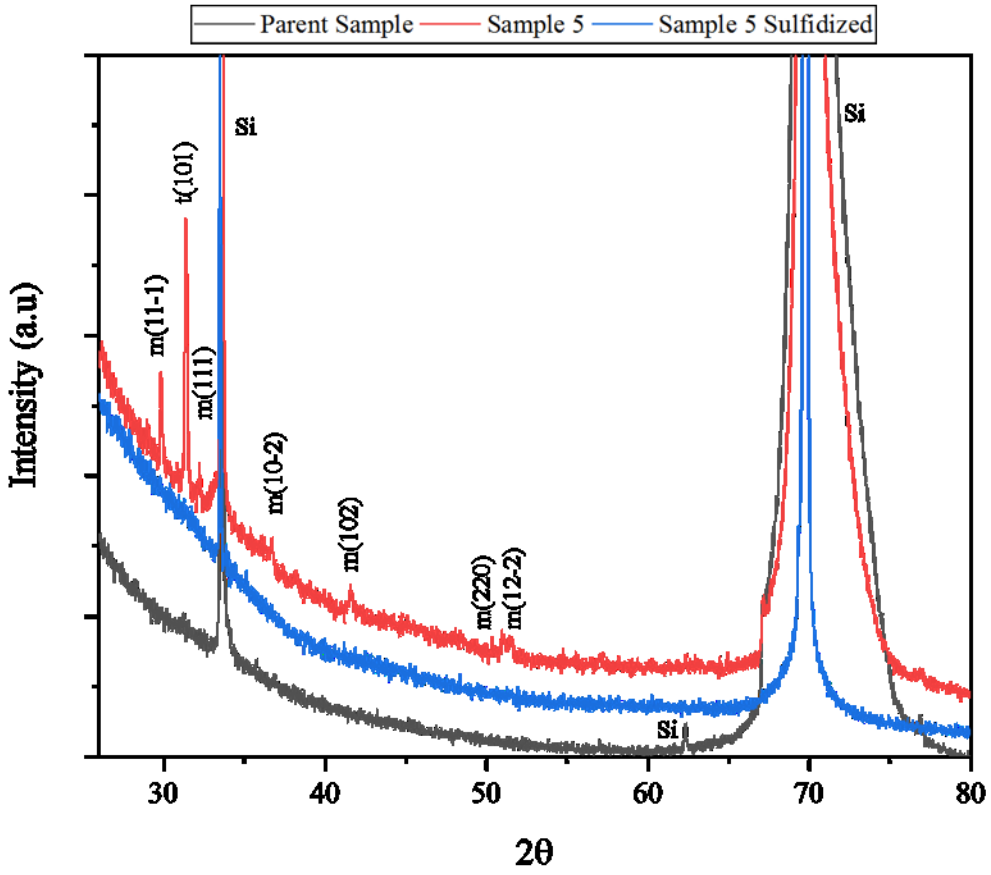


Figure 3.4: XRD graph of ALD-grown sample 5 HfO2 on silicon.

After a final annealing, minor monoclinic peaks appear with different orientations (as indicated by the arrows in figure 3.5a), and the orthorhombic peak (~25.8°) (in figure 3.5b) shows a significant increase in intensity. At ~53.6°, two monoclinic peaks are present with an orientation of (122) and (11-3), respectively, and a broad m(200) at ~35.6°. For the orthorhombic peak at ~25.8°, there are certain conditions in which the orthorhombic phase may occur. Since the annealing temperature and pressure parameters are nearly identical with that of sample 5, it is reasonable to assume that there are other factors involved with the formation of the orthorhombic

structure in sample 16. The orthorhombic phase will be discussed in detail further in this chapter. For now, I will focus on the sulfidation and peak position at ~72° for sample 16, and sample 18.

For sample 16, sulfidation was performed with the same parameters as sample 5: 0.1M of Thiourea at 180°C. However, the sulfidation time was 8 hours instead of 16 hours. From figure 3.5a, the sample transitioned from a polycrystalline phase back to a mostly amorphous phase similar to the parent sample after sulfidation. A final annealing was done at 500°C in argon atmosphere at a pressure of 1.0E-1 mbar. This final annealing after sulfidation causes the amorphous structure to transition to a polycrystalline phase, as shown in figure 3.5a.

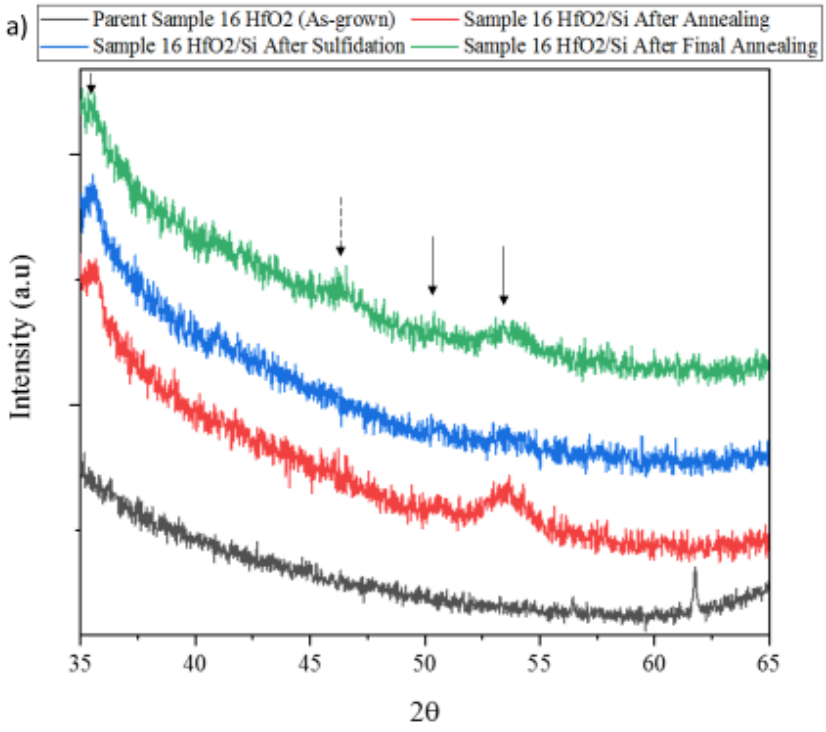


Figure 3.5a: XRD plot of sample 16 of the ALD-grown thin film on silicon substrate. This plot only shows the minor peaks at the XRD θ-2θ range of 35°-65°.

However, an additional peak is present at ~71° as shown by the dotted arrow in figure 3.5b. Deconvolution of this peak is shown in figure 3.6. From figure 3.6a, peak deconvolution shows 4 fitted peaks. Fit Peak 2 & 3 refer to the silicon substrate. If these peaks are omitted, then Fit Peak 1 & 4 remain with the peaks positioned at 69.13° and 70.67°, respectively. Fit Peak 1 in figure 3.6a has the same peak position as Fit Peak 2, which is Si(400) $K\alpha_1$. This peak is also present after the first annealing of the parent sample, as denoted by the arrow in the inset graph of figure 3.6b.

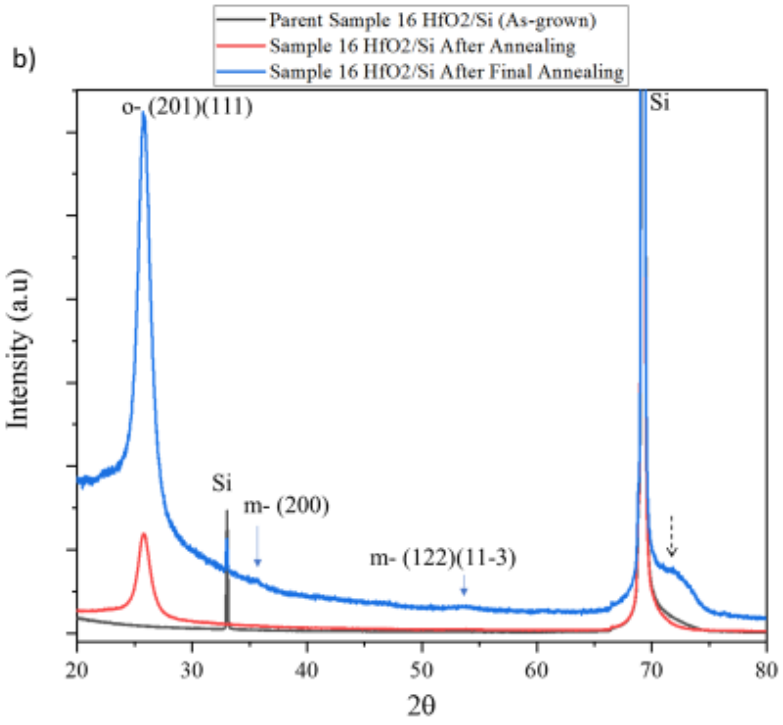


Figure 3.5b: Full XRD scan of sample 16. Only the results from the parent sample, first annealing, and final annealing are shown. An errored during the XRD scan for the sulfidised film. Therefore, that particular plot was omitted.

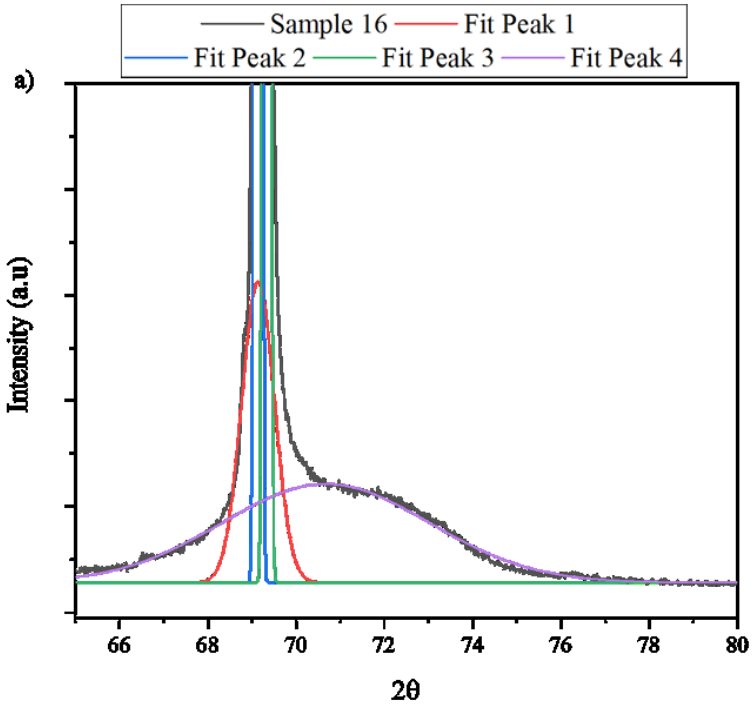


Figure 3.6a: The four fitted peaks show 2 silicon peaks, and two additional peaks.

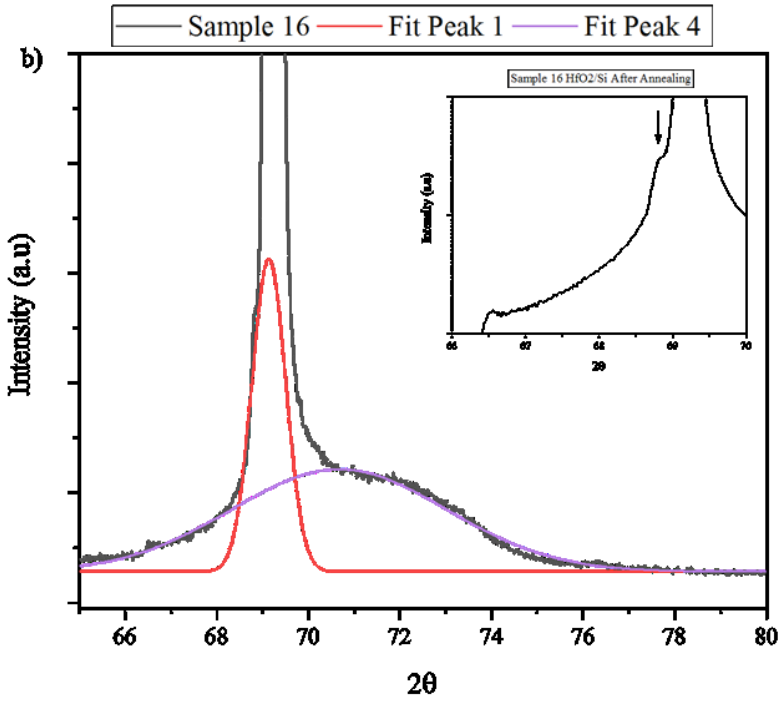


Figure 3.6b: Omitting the silicon peaks for further analysis shows Fit Peak 1 at 69.13°, and Fit Peak 4 at 70.67°. The inset shows a peak (arrow) after the first annealing.

The more interesting peak is at 70.67°. Figures 3.7a-d show the peak (Fit Peak 4) overlaid with individual CIF cards. The ICSD CIF cards that correspond to h-HfS2, c-HfS3, m-HfO2, and m-HfOS crystal structures are 43203, 638846, 27313, and 23327 respectively. Fit peak 4 is broad enough to be of mixed phase or possess a combination of different crystal structures such as h-HfS2, c-HfS3, m-HfO2, or m-HfOS. The reason for the mixed phase is due to it also having the same peak position as orthorhombic $HfO_2$ (not pictured) in the (711) direction. Thus, the peak could be monoclinic and orthorhombic, as well as a mixture of any of the other crystal structures. Figure 3.7d shows a peak in the (31-4) direction, which is also in the same position of Fit Peak 4, 70.67°. For this position, the intensity from the o-$HfO_2$ ICSD 79913 CIF card is miniscule and similar in intensity as the m-$HfS_3$ (31-4) peak shown in figure 3.7d.

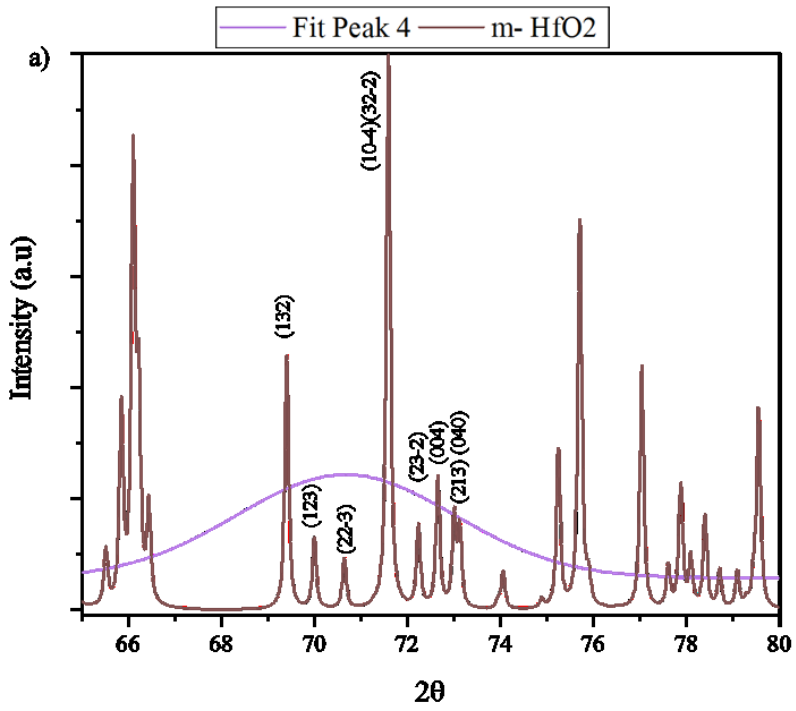


Figure 3.7a: Shows Fit Peak 4 overlaid with the CIF file m-HfO2 taken from the ICSD database.

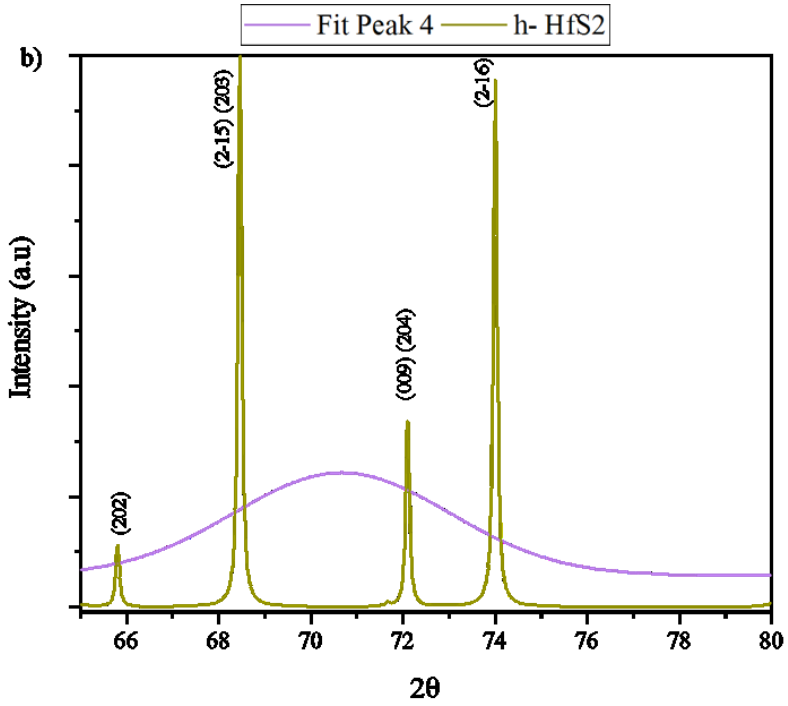


Figure 3.7b: Shows Fit Peak 4 overlaid with the CIF file h-HfS2 taken from the ICSD database.

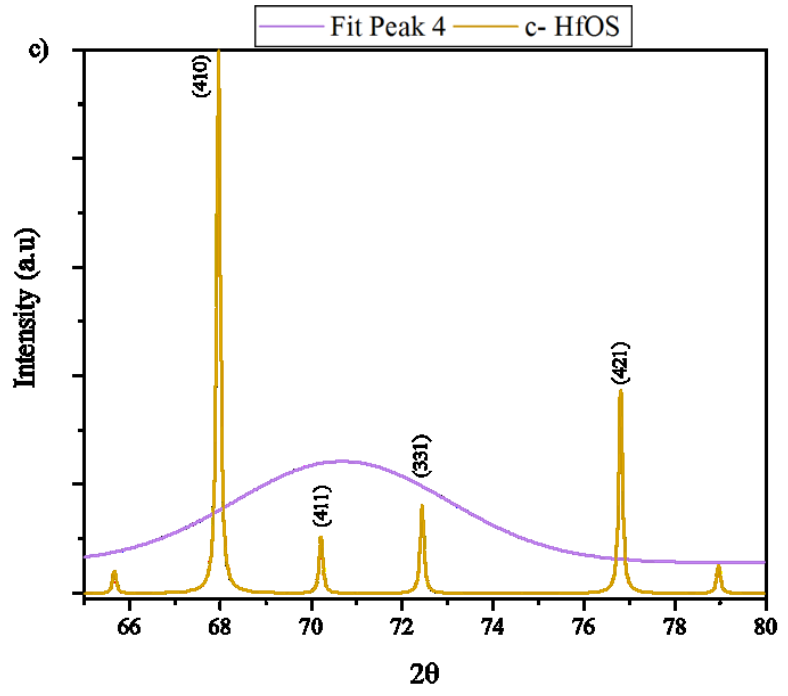


Figure 3.7c: Shows Fit Peak 4 overlaid with the CIF file c-HfOS taken from the ICSD database.

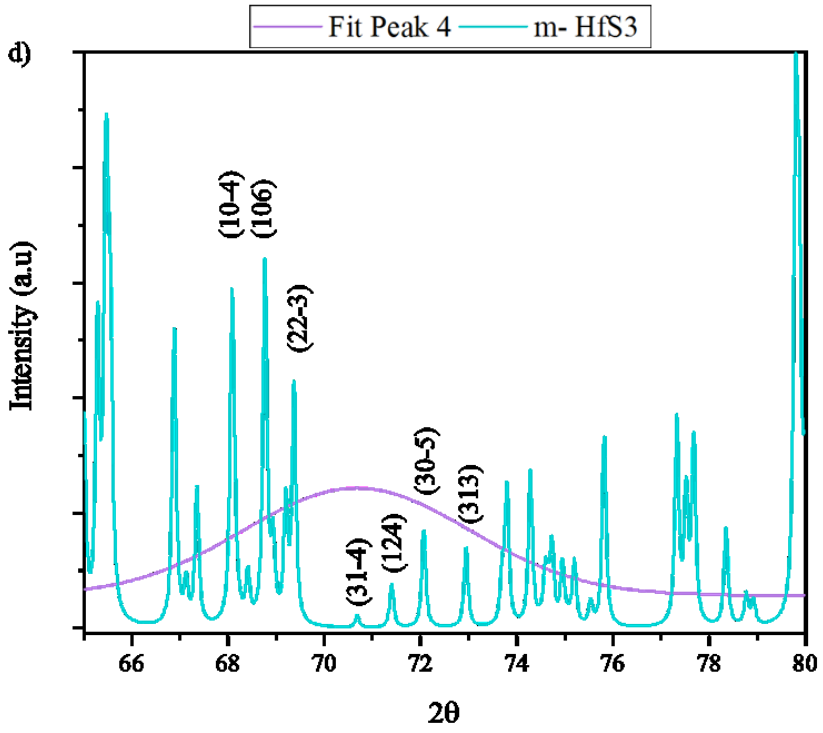


Figure 3.7d: Shows Fit Peak 4 overlaid with the CIF file m-HfS3 taken from the ICSD database.

Figure 3.8 for sample 18 shows the familiar dominant orthorhombic peak (as was the case with sample 16) at ~25.8°, and minor monoclinic peaks between 35° - 60° after final annealing. sample 18 also shows a shoulder peak (as indicated by the dotted arrow) at ~72°, indicating the formation of h-$HfS_2$, c-$HfS_3$, m-$HfO_2$, m-HfOS, a combination thereof, and/or a mixed phase of orthorhombic and monoclinic. Note that this peak is not present until after the sample has been annealed in argon atmosphere (1.0E-1 mbar) at 500°C for 1 hour. (An attempt was made to deconvolute this peak, but it simply wasn't possible with the dominant substrate peak present.) In addition, the forbidden silicon peak at ~33° is not present after sulfidation. However, it does reappear after final annealing. Annealing improves the crystallinity of the substrate, giving it the well-defined in-plane orientation required for the forbidden reflection peak to reappear.

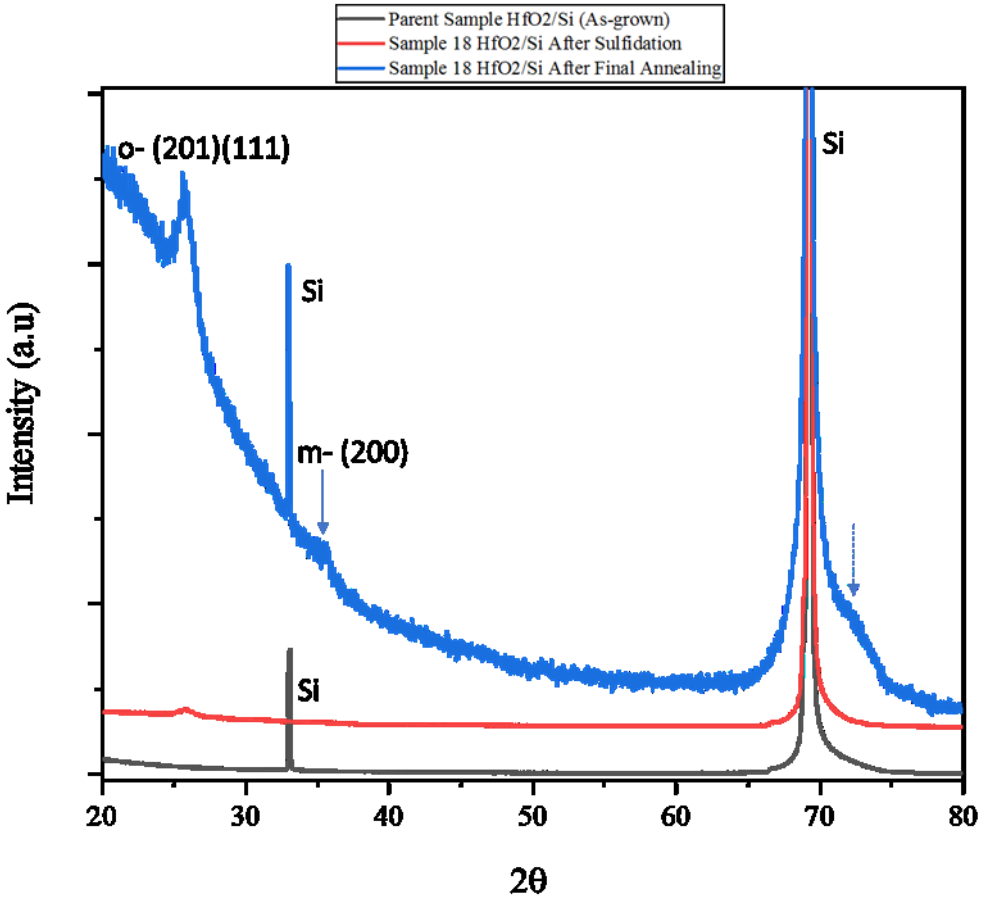


Figure 3.8: Sample 18 of ALD-grown HfO2/Si. The dotted arrow at ~72° indicates the new convoluted peak that denotes a mixed phase of $HfO_2$, hafnium oxysulfide, or a combination thereof after annealing the sulfidised sample.

Sample 5 was sulfidised in early 2019, whereas sample 16 and sample 18 were sulfidised in December of 2019. Although the parent sample was stored in a secure area where it would not be exposed to additional elements, it may be possible that sample 16 and sample 18 became contaminated during this time frame. Another plausible explanation is that the vacuum chamber where annealing took place may have been contaminated with a foreign chemical within the span of several months. However, the orthorhombic peak is always present regardless of whether the sample was annealed first, or sulfidised first. Park *et al*. reported that the formation of the

orthorhombic phase could be due to surface/interfacial energy effects, size effects, dopant concentration, and/or stress/strain in the thin films.[35]

Raman spectroscopy is used to study the vibrational, rotational, and other low frequency transitions in molecules. It is based on the inelastic scattering of monochromatic light. This means that the frequency of photons in the monochromatic light changes upon interaction with the sample and is then reemitted. The frequency of the emitted photon can shift either up or down when compared with the original frequency. This is known as the Raman effect. The scattering of light studied in this paper is known as Stokes scattering, and is the shift up from the original frequency. Raman spectroscopy was performed with a Horiba LabRAM HR Confocal Raman microscope on the silicon substrate, parent sample, sample 5, 16, and 18.

Uchinokura *et al*. reported the first and second-order Raman spectra of silicon which includes one-phonon structure and two-phonon weak structure. The main first order peak was located at 520 $cm^{-1}$, and an intense second-order broad band was located between 920 $cm^{-1}$ and 1045 $cm^{-1}$. However, the entire two-phonon spectrum was observed between 600$cm^{-1}$ and 1045 $cm^{-1}$.[36] Spizzirri *et al*. also reported the first and second-order Raman spectrum of silicon. Their results indicated that the first order peak position was at 520 $cm^{-1}$ which arises from the creation of the long wavelength transverse optical phonon (TO). The second-order spectrum is much weaker and ranges from 0 to 1050 $cm^{-1}$.[37]

Borowicz *et al*. reported the silicon first-order Raman band at 520 $cm^{-1}$ and the "multi-phonon" band between 930 $cm^{-1}$ and 1030 $cm^{-1}$. They also reported that the bands for the as-deposited $HfO_2$ are merged in such a way that the main band placed between 300 $cm^{-1}$ and 550 $cm^{-1}$ has a tail that extends to 930 $cm^{-1}$. Their results also state that this band is similar for spectra recorded for $SiO_2$ and $HfO_2$ as-deposited films. Wu *et al*. reported that the $HfO_2$ Raman

modes observed in the 130 $cm^{-1}$ – 270 $cm^{-1}$ are mainly assigned to the vibrations of hafnium atoms, while the Raman modes above 270 $cm^{-1}$ are related to the vibrations in which the oxygen atoms are actively participating. The Hf atoms will show smaller displacements than $O_1$ and $O_2$ atoms due to the weight ratio.[38,39] It should be noted that all Raman modes of $HfO_2$ vary between LDA, GGA, and experimental values, and can deviate as much as 13% at greater frequencies.[40]

The first-order Raman-active mode for hafnium disulfide was also studied. Cingolani *et al.* reported $HfS_2$ Raman-active modes $E_g$ at 260 $cm^{-1}$ and $A_{1g}$ at 337 $cm^{-1}$. Kanazawa *et al*. also observed the Raman-active mode $A_{1g}$ at 337 $cm^{-1}$, while Chen reported that the calculated $A_{1g}$ mode for bulk as well as monolayer is 331 $cm^{-1}$. In addition, Chen reported the calculated $E_g$(LO) and $E_g$(TO) to be 265 $cm^{-1}$, respectively, for monolayer $HfS_2$. The frequencies bulk $HfO_2$ for these 2 modes deviated only by 0.3% (264 $cm^{-1}$). Experimentally, the $A_{1g}$ value is 337 $cm^{-1}$, as quoted by Chen, and is in accordance with the calculated value. The $A_{7g}$ mode has the strongest line at 495 $cm^{-1}$ in the simulated spectrum, as reported by Wu *et al*. Although it is in good agreement with the experimental value of 498 $cm^{-1}$, the silicon TO mode has such a strong intensity in my results that peak deconvolution of this line wasn't possible.[27,41,42]

From figure 3.9, the first-order transverse optical (TO) phonon mode located at 520.7 $cm^{-1}$ is from the silicon substrate. The second-order Raman active modes 2TA, 2LA, 2LO, and 2TO for silicon are located between 300-1100 $cm^{-1}$, and the recorded spectra from my experiment is nearly identical to that of Spizzirri *et al*. Table 4 shows the 18 theoretical Raman-active modes for monoclinic hafnia. Figure 3.10 shows the spectrum from 100 $cm^{-1}$ to 800 $cm^{-1}$ and several first-order $HfO_2$ $A_g/B_g$ peaks are labeled. There are a couple noticeable differences between the silicon substrate and "$HfO_2$ After Annealing". The Raman-active modes $A_{1g}$ + $B_{1g}$ peak at ~128 $cm^{-1}$, and the $B_{2g}$ peak at 131 $cm^{-1}$ are more prominent when comparing the silicon substrate with

"Sample 5 $HfO_2$/Si After Annealing". Wu *et al*. also saw this ambiguity due to the frequencies being so close together and the modes having comparable strengths. Their calculated LDA values are listed on table 4. There is also a noticeable difference in the "After Annealing" peak shape for the $A_{9g}$ and $B_{8g}$ modes at ~640 $cm^{-1}$ when compared with the substrate. The GGA calculated value for $A_{9g}$ is 640 $cm^{-1}$ and is in agreement with the experimental results reported by Tkachev *et al*. (The Raman plot of the silicon substrate is omitted in figure 3.11 and 3.12 due to the fact that the parent sample is the same for all samples, so the comparisons with as-grown samples would be redundant with sample 5.)[43]

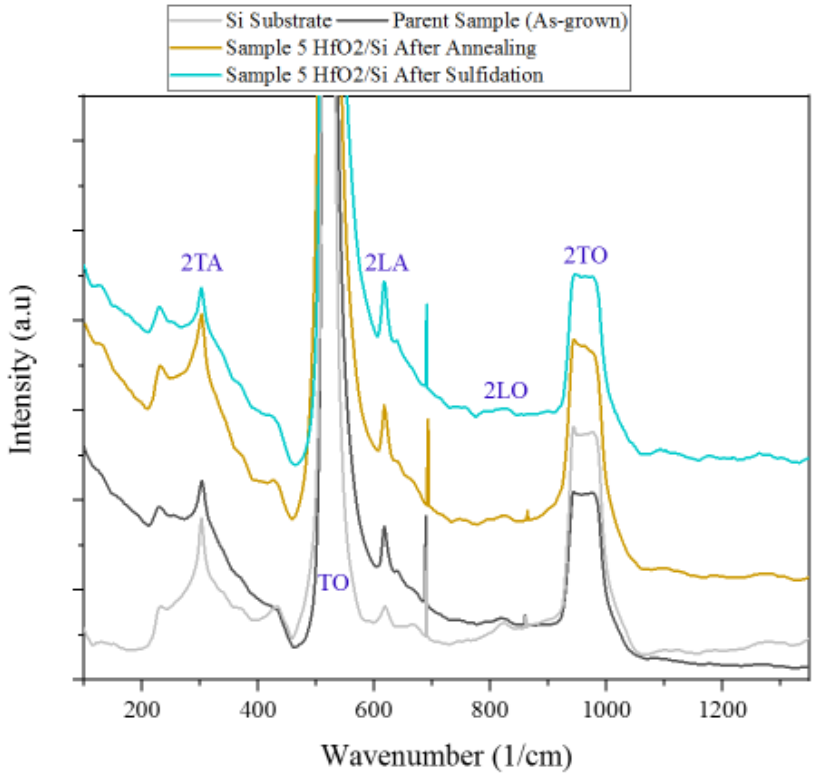


Figure 3.9: Raman spectra of silicon substrate, hafnia parent sample, and sample 5. The blue labels refer to the Raman-active modes of the silicon substrate.

After sulfidation of sample 5, figure 3.10 shows a subtle $HfS_2$ first-order $A_{1g}$ peak at 337 $cm^{-1}$. The $E_g$ peak at 264 $cm^{-1}$ is more prominent, but some ambiguity remains due to the

possibility that the peak can be the result of low resolution of the spectrometer or is simply weak in intensity when compared with the Raman-active silicon. Along with $E_g$, the $A_{4g}$ mode can also be a possibility for the minor peak at 264 $cm^{-1}$.

Table 4: Theoretical and Experimental[5,40] m-$HfO_2$ Raman-active modes

| Mode | LDA | GGA | Exp[5,40] | Mode | LDA | GGA | Exp[5,40] |
|---|---|---|---|---|---|---|---|
| $A_{1g}$ | 128 | 125 | 113 | $B_{1g}$ | 131 | 120 | 133 |
| $A_{2g}$ | 142 | 132 | 133 | $B_{2g}$ | 175 | 152 | 164 |
| $A_{3g}$ | 152 | 171 | 149 | $B_{3g}$ | 250 | 223 | 242 |
| $A_{4g}$ | 261 | 248 | 256 | $B_{4g}$ | 380 | 318 | 336 |
| $A_{5g}$ | 326 | 339 | 323 | $B_{5g}$ | 424 | 385 | 398 |
| $A_{6g}$ | 423 | 382 | 382 | $B_{6g}$ | 533 | 466 | 520 |
| $A_{7g}$ | 514 | 440 | 498 | $B_{7g}$ | 570 | 529 | 551 |
| $A_{8g}$ | 608 | 557 | 577 | $B_{8g}$ | 667 | 627 | 640 |
| $A_{9g}$ | 738 | 640 | 672 | $B_{9g}$ | 821 | 716 | 872 |

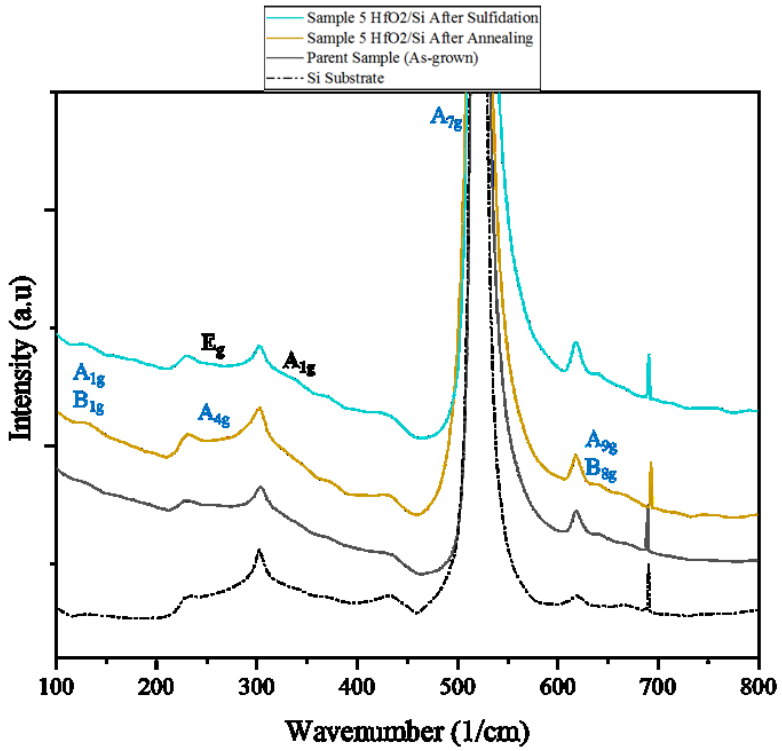


Figure 3.10: Labeled Raman-active $HfS_2$ (dark bold) and $HfO_2$ (blue) modes for sample 5.

For sample 16, after final annealing of the parent sample, it shows the $A_{1g}/B_{1g}$ Raman modes in figure 3.11, as well as the $A_{9g}/B_{8g}$ when compared to the silicon substrate (not shown). The $A_{4g}$ mode is difficult to ascertain in the After Annealing plot. This is most likely due to poor resolution of the Raman scan. The $A_{7g}$ peak is also difficult to determine due to the high intensity of the TO mode of the silicon substrate. For "Sample 16 After Final Annealing", the weak $E_g$ mode for $HfS_2$ is present without any ambiguity. Although the $HfS_2$ $A_{1g}$ mode appears to be present in the After Sulfidation plot, the peak appears broad in the "After Final Annealing" plot.

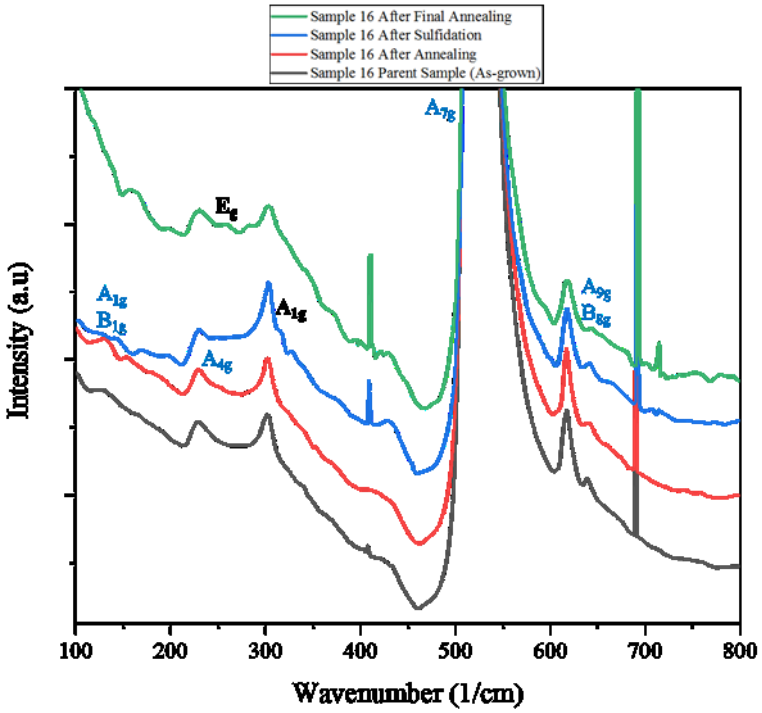


Figure 3.11: Labeled Raman-active $HfS_2$ (dark bold) and $HfO_2$ (blue) modes for sample 16.

From figure 3.12, sample 18 shows results similar to sample 16 for the "After Final Annealing" plot. The first order Raman modes of $HfS_2$ are present, and with the same difference

in peak intensity. Recall that "After Final Annealing" refers to annealing the sample after sulfidation.

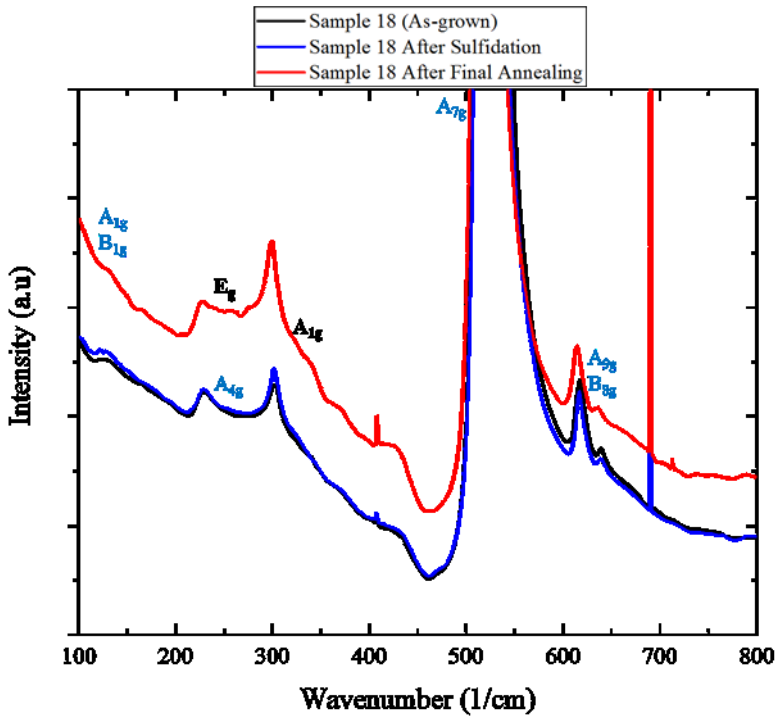


Figure 3.12: The labeled Raman-active $HfS_2$ (dark bold) and $HfO_2$ (blue) modes for sample 18.

Figure 3.13 shows the Raman spectra for hafnia on $Al_2O_3$ before and after sulfidation. Raman spectroscopy was performed at the Wright-Patterson Air Force Research Laboratory using a Renishaw inVia Qontor confocal Raman microscope. Raman modes corresponding to $HfS_2$ and hafnia are labeled, as reported by Cingolani *et al*. and Wu *et al.* The first-order vibrational mode of $HfS_2$ is clearly evident after sulfidation of hafnia with $E_g$ at ~234 $cm^{-1}$, and $A_{1g}$ at ~337 $cm^{-1}$. The second order Raman bands located at approximately 670, 640, 620, 586, and 498 $cm^{-1}$ are denoted with arrows in figure 3.13. There is an obvious difference in intensity at each of these positions in comparison with the PLD-grown Raman spectrum before sulfidation

and the sapphire substrate. These peaks can only come from $HfS_2$ since their presence is not present in the hafnia plot. The more evident vibrational modes of hafnia are also labeled appropriately.[39,41] Annealing of the sample may further deconvolute the first-order $HfO_2$ and first-order $HfS_2$ peaks.

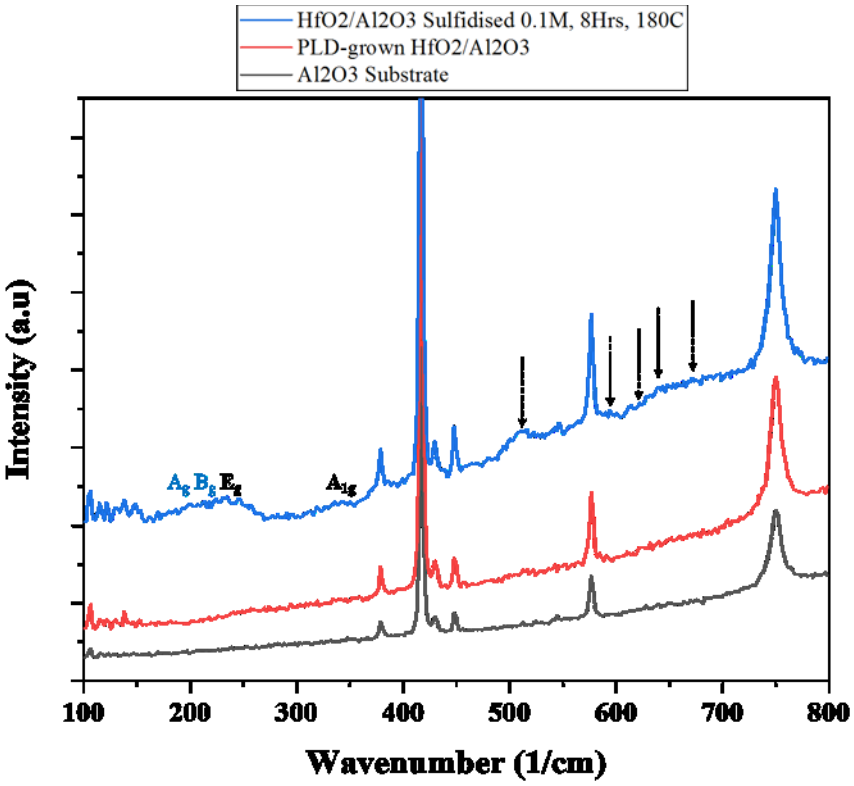


Figure 3.13: Raman spectrum of PLD-grown hafnia before and after sulfidation. The first order Raman-active modes for $HfS_2$ (dark bold) and $HfO_2$ (blue) modes are labeled. The arrows denote the positions of the second-order Raman bands for $HfS_2$ at approximately 670, 640, 620, 586, and 498 $cm^{-1}$.

**Conclusions**

Current methods, such as mechanical exfoliation and chemical transport, aren't practical enough to be considered wide-scale fabrication techniques. A method that was investigated throughout this thesis is hydrothermal synthesis for the creation of $HfS_2$ layers on $HfO_2$. After

the creation of hafnia via PLD and ALD, sulfidation of the samples was performed via hydrothermal synthesis. The characterization of the sulfidised samples was conducted using X-ray diffraction (XRD) and Raman spectroscopy. From the XRD data, it is apparent that the broad peak at ~71° is related to hafnium oxysulfide, which can consist of m-$HfO_2$, o-$HfO_2$, $HfS_2$, Hf-OS, and/or $HfS_3$, or a combination thereof. The Raman spectra of ALD-grown hafnia after sulfidation indicates that the vibrational modes of $HfS_2$ are present after annealing of sulfidised samples 16 and 18. The Raman spectrum of the PLD-grown sample also shows $HfS_2$ first-order vibrational modes, as well as multiple second-order Raman bands. Analysis using Transmission Electron Microscopy (TEM) would be the next logical step in determining the crystal structure and thickness of the $HfS_2$ layer after 8 and 16 hours of sulfidation. The development of the new materials using this newly-established technique can possibly lead to lower power consumption, lower cost, improved efficiency, and faster response time for electronic devices.

# CONCLUSIONS AND FUTURE WORK

Using hydrothermal synthesis, the $HfO_2/HfS_2$ heterostructure was synthesized successfully, and verified with Raman spectroscopy and X-ray diffraction. It has also been shown that annealing after sulfidation of the ALD-grown samples further enhances the XRD peak at ~71°, which is related to hafnium oxysulfide -a combination of $HfO_2$, $HfS_2$, or mixed phase containing oxygen and/or sulfur. The PLD-grown sample shows an unambiguous first-order Raman mode after sulfidation, while the ALD-grown samples are ambiguous due to low resolution of the spectrometer, or a high intensity of the silicon modes. Dielectric spectroscopy of the hafnia samples shows that the dielectric constant (at 1kHz) can vary depending on the ohmic conductivity of the LCR probes. Improvement in the etching process for the contact probes, and an increase in the frequency range (to microwave/IR) would be beneficial to understanding the frequency-dependent polarization of $HfO_2$. To further investigate the $HfO_2/HfS_2$ heterostructure, TEM analysis would prove to be beneficial in understanding the morphology of the heterojunction, and the mechanism that drives the hydrothermal synthesis process. Also, the rate of hydrothermal synthesis can be ascertained by conducting sulfidation experiments at different intervals and analyzing the $HfO_2/HfS_2$ heterostructure via TEM.

## REFERENCES


1. Geim, A. K. Graphene prehistory. *Phys. Scr.* (2012) doi:10.1088/0031-8949/2012/T146/014003.

2. Choi, W. *et al.* Recent development of two-dimensional transition metal dichalcogenides and their applications. *Materials Today* (2017) doi:10.1016/j.mattod.2016.10.002.

3. Mistry, K. *et al.* A 45nm logic technology with high-k+ metal gate transistors, strained silicon, 9 Cu interconnect layers, 193nm dry patterning, and 100% Pb-free packaging. in *Technical Digest - International Electron Devices Meeting, IEDM* (2007). doi:10.1109/IEDM.2007.4418914.

4. Dole, S. L. Elastic properties of monoclinic hafnium oxide. 129 (1977).

5. Zhao, X. & Vanderbilt, D. First-principles study of structural, vibrational, and lattice dielectric properties of hafnium oxide. *Phys. Rev. B - Condens. Matter Mater. Phys.* (2002) doi:10.1103/PhysRevB.65.233106.

6. Böscke, T. S., Müller, J., Bräuhaus, D., Schröder, U. & Böttger, U. Ferroelectricity in hafnium oxide thin films. *Appl. Phys. Lett.* (2011) doi:10.1063/1.3634052.

7. P., A., C., Z. & K., P. Hafnium-based High-k Gate Dielectrics. in *Advances in Solid State Circuit Technologies* (2010). doi:10.5772/8631.

8. Houssa, M. *High-k Gate dielectrics*. *High-K Gate Dielectrics* (2003). doi:10.1201/9780429086335-4.

9. Gao, L. *et al.* Effect of oxygen vacancies and strain on the phonon spectrum of HfO2 thin films. *J. Appl. Phys.* (2017) doi:10.1063/1.4984833.

10. Ramalingam, G. *et al.* Quantum Confinement Effect of 2D Nanomaterials. in *Quantum Dots - Fundamental and Applications* (2020). doi:10.5772/intechopen.90140.

11. Lai, S. *et al.* HfO2/HfS2 hybrid heterostructure fabricated: Via controllable chemical conversion of two-dimensional HfS2. *Nanoscale* **10**, 18758–18766 (2018).

12. Dissado, L. Dielectric response. in *Springer Handbooks* (2017). doi:10.1007/978-3-319-48933-9_10.

13. Kittel, C. Introduction to Solid State Physics, 8th edition. *Wiley Sons, New York, NY* (2004).

14. Laughton, M. A. & Warne, D. F. *Electrical Engineer's Reference Book: Sixteenth Edition*. *Electrical Engineer's Reference Book: Sixteenth Edition* (2003).

15. Bands, R. http://www.horiba.com/fileadmin/uploads/Scientific/Documents/Raman/bands.pdf. *Horiba Sci.* (2011).

16. Princeton Instruments. Raman Spectroscopy Basics - Application Note. *Internet: http://content. piacton. com/Uploads/Princeton/* (2012).

17. Choi, W. *et al.* Recent development of two-dimensional transition metal dichalcogenides and their applications. *Materials Today* (2017) doi:10.1016/j.mattod.2016.10.002.

18. Robertson, J. Interfaces and defects of high-K oxides on silicon. *Solid-State Electronics* (2005) doi:10.1016/j.sse.2004.11.011.

19. Zhang, X. Y. *et al.* Temperature-Dependent HfO2/Si Interface Structural Evolution and its Mechanism. *Nanoscale Res. Lett.* (2019) doi:10.1186/s11671-019-2915-0.

20. Robertson, J. High dielectric constant oxides. *EPJ Applied Physics* (2004) doi:10.1051/epjap:2004206.

21. Ho, M. Y. *et al.* Morphology and crystallization kinetics in HfO2 thin films grown by atomic layer deposition. *J. Appl. Phys.* (2003) doi:10.1063/1.1534381.

22. Katamreddy, R., Inman, R., Jursich, G., Soulet, A. & Takoudis, C. Atomic layer

deposition of HfO2, Al2O3, and HfAlOx using O3 and metal(diethylamino) precursors. *J. Mater. Res.* (2007) doi:10.1557/jmr.2007.0439.

23. Ritala, M. *et al.* Development of crystallinity and morphology in hafnium dioxide thin films grown by atomic layer epitaxy. *Thin Solid Films* (1994) doi:10.1016/0040-6090(94)90168-6.

24. Widjaja, Y. & Musgrave, C. B. Atomic layer deposition of hafnium oxide: A detailed reaction mechanism from first principles. *J. Chem. Phys.* (2002) doi:10.1063/1.1495847.

25. He, G. *et al.* Effect of postdeposition annealing on the thermal stability and structural characteristics of sputtered HfO2 films on Si (1 0 0). *Surf. Sci.* (2005) doi:10.1016/j.susc.2004.11.042.

26. Okada, K. & Sekino, T. *Impedance Measurement Handbook, Keysight Technologies*. *Keysight Technologies* (2016).

27. Kanazawa, T. *et al.* Few-layer HfS2 transistors. *Sci. Rep.* (2016) doi:10.1038/srep22277.

28. Kanazawa, T. *et al.* Performance Improvement of HfS2 Transistors by Atomic Layer Deposition of HfO2. *IEEE Trans. Nanotechnol.* (2017) doi:10.1109/TNANO.2017.2661403.

29. Sahu, S., Rani Sahoo, P., Patel, S. & Mishra, B. K. Oxidation of thiourea and substituted thioureas: A review. *Journal of Sulfur Chemistry* (2011) doi:10.1080/17415993.2010.550294.

30. Lu, Z. *et al.* In situ fabrication of porous MoS2 thin-films as high-performance catalysts for electrochemical hydrogen evolution. *Chem. Commun.* (2013) doi:10.1039/c3cc44143a.

31. Nie, X. *et al.* Facile hydrothermal synthesis of nanocubic pyrite crystals using greigite fe3s4 and thiourea as precursors. *Minerals* (2019) doi:10.3390/min9050273.

32. Yang, G. & Park, S. J. Conventional and microwave hydrothermal synthesis and application of functional materials: A review. *Materials* (2019) doi:10.3390/ma12071177.

33. Okamura, K., Nasr, B., Brand, R. A. & Hahn, H. Solution-processed oxide semiconductor SnO in p-channel thin-film transistors. *J. Mater. Chem.* (2012) doi:10.1039/c2jm16426d.

34. Zaumseil, P. High-resolution characterization of the forbidden Si 200 and Si 222 reflections. *J. Appl. Crystallogr.* (2015) doi:10.1107/S1600576715004732.

35. Park, M. H. *et al.* A comprehensive study on the structural evolution of HfO2 thin films doped with various dopants. *J. Mater. Chem. C* (2017) doi:10.1039/c7tc01200d.

36. Uchinokura, K., Sekine, T. & Matsuura, E. Raman scattering by silicon. *Solid State Commun.* (1972) doi:10.1016/0038-1098(72)91127-1.

37. Spizzirri, P. G., Fang, J. H., Rubanov, S., Gauja, E. & Prawer, S. Nano-Raman spectroscopy of silicon surfaces. in *Materials Forum* (2008).

38. Borowicz, P., Taube, A., Rzodkiewicz, W., Latek, M. & Gierałtowska, S. Raman spectra of high-κ dielectric layers investigated with micro-raman spectroscopy comparison with silicon dioxide. *Sci. World J.* (2013) doi:10.1155/2013/208081.

39. Wu, R. *et al.* Elastic and vibrational properties of monoclinic HfO 2 from first-principles study. *J. Phys. D. Appl. Phys.* (2012) doi:10.1088/0022-3727/45/12/125304.

40. Arashi, H. Pressure-Induced Phase Transformation of HfO2. *J. Am. Ceram. Soc.* (1992) doi:10.1111/j.1151-2916.1992.tb04149.x.

41. Cingolani, A., Lugará, M., Scamarcio, G. & Lévy, F. The Raman scattering in hafnium disulfide. *Solid State Commun.* (1987) doi:10.1016/0038-1098(87)91126-4.

42. Chen, J. Phonons in bulk and monolayer HfS2 and possibility of phonon-mediated superconductivity: A first-principles study. *Solid State Commun.* (2016) doi:10.1016/j.ssc.2016.03.021.

43. Tkachev, S. N., Manghnani, M. H., Niilisk, A., Aarik, J. & Mändar, H. Raman and Brillouin scattering spectroscopy studies of atomic layer-deposited ZrO2 and HfO2 thin films. in *Spectrochimica Acta - Part A: Molecular and Biomolecular Spectroscopy* (2005). doi:10.1016/j.saa.2005.02.025.